SAND2020-9397B

Chapter 1.

Dynamic High-Rate Tensile Characterization of Metallic Materials with a Kolsky Tension Bar

Bo Song, Brett Sanborn

Sandia National Laboratories, Albuquerque, NM, United States

Introduction

Metallic materials are ubiquitous and indispensable to daily life due to their excellent manufacturability as well as their relatively high strength and ductility. Some metallic materials also exhibit notable corrosion resistance, weldability, recyclability, and reusability, which renders them suitable for broad applications such as architecture, food, medical, civil, energy, automotive, aerospace, and defense industries. In such applications, components made of metallic materials may be subjected to abnormal or extreme mechanical environments ranging from low-speed drop to high-speed impact, crash, shock or explosion. Assessment of safety and reliability of components under such conditions becomes paramount, with the dynamic stress-strain response including failure and fracture being key parameters. The material response information can be used to develop strain-rate-dependent material models to enable predictive simulations to evaluate the safety and reliability of a component under extreme conditions.

Experimental methods to investigate the dynamic stress-strain response of metallic materials have been developed over the past several decades in both compression and tension. Compared to studies of dynamic compressive material behavior, the dynamic tensile behavior of metallic materials has been less studied due to limited experimental technique development. Dynamic tension studies have not only challenges in effectively loading the sample, but complexities in deformation or strain measurements as well. An ideal dynamic tension experiment would reveal the full material stress-strain behavior including yield, ductility and necking, as well as failure and fracture properties. In the past, ring expansion [1-4], cap expansion [5], spall [6-8], and dynamic tensile extrusion [9-13] techniques have been introduced to investigate dynamic tensile failure and fractography, but have not provided the stress-strain curves needed to construct constitutive models. The Kolsky bar, also called the split-Hopkinson bar, has been an efficient and effective tool to determine the stress-strain response of materials at high strain rates since it was established for compression experiments by Kolsky in 1949 [14]. The first Kolsky tension bar was developed by Harding et al. [15] in 1960 and has subsequently undergone many modifications and improvements for dynamic material characterization at high strain rates. Since then, Kolsky tension bar techniques have seen both less development and documentation compared to Kolsky compression bar techniques, though a few review articles have been published [16-18]. For example, in their book, *The Kolsky Bar*, Chen and Song [18] presented detailed dynamic compression experimental techniques for a variety of conditions and materials, but only dedicated a

Sandia National Laboratories is a multimission laboratory managed and operated by National Technology & Engineering Solutions of Sandia, LLC, a wholly owned subsidiary of Honeywell International Inc., for the U.S. Department of Energy's National Nuclear Security Administration under contract DE-NA0003525.

single chapter to dynamic tensile techniques. The past decade has seen a significant progression in Kolsky tension bar methods. Therefore, now is an opportune time to systematically summarize the progress in dynamic tensile characterization techniques.

In this chapter, we present detailed Kolsky tension bar design, tensile specimen design and mounting methods, diagnostic and measurement methods, as well as data interpretation.

Kolsky Tension Bar Design and Testing Challenges

Compared to Kolsky compression bars, Kolsky tension bar designs are more diversified, but all follow the same principle. Several different methods have been developed to generate dynamic tensile loading pulses. In the first tension bar established in the 1960s, a hollow tube was connected to a yoke and threaded specimen inside the tube. A tensile wave was generated at the free end after the tube was impacted externally in compression [15, 19]. This method was further modified by Harding and Welsh [20] by placing an additional bar between the tensile specimen and the end of the tube. In this design, the tube served as a loading device while the added bar served as an incident bar. Following a similar concept, a load inversion device was developed to dynamically load a metallic sheet specimen in tension with a compressive loading pulse [21-23]. Lindholm and Yeakley [24] designed a "top-hat" specimen and applied it to a Kolsky compression bar for dynamic tensile property characterization. Nicholas [25] used a typical compression setup to generate tensile loading with a specially designed collar around the specimen. The rigid collar allowed the compressive wave to transmit into the transmission bar but prevented the specimen from being loaded in compression. The compressive wave was reflected at the free end of the transmission bar as a tensile wave, which then subjected the specimen to dynamic tension. All dynamic tensile tests above basically use the Kolsky compression bar device for dynamic tensile characterization. Some of these methods are still being used but in a limited manner [26-28].

In the past few decades, direct tensile impact techniques have been developed for high-strain-rate tensile characterization of materials. These methods use different loading mechanisms including a drop weight [29] or a flying wedge [30, 31]. Other loading mechanisms were also implemented with Kolsky bars to directly generate tensile waves, forming true Kolsky tension bars. Except for rotating-disk or impact-hammer-driven setups [32-37], and the more recently developed electromagnetically driven [38] Kolsky tension bars, there are currently three mainstream Kolsky tension bar designs that include pre-stretched Kolsky tension bars (Fig. 1.1(a)) [39-51], Kolsky tension bars with a tubular striker (Fig. 1.1(b)) [52-76], and Kolsky tension bars with a solid striker (Fig. 1.1(c)) [77-85].

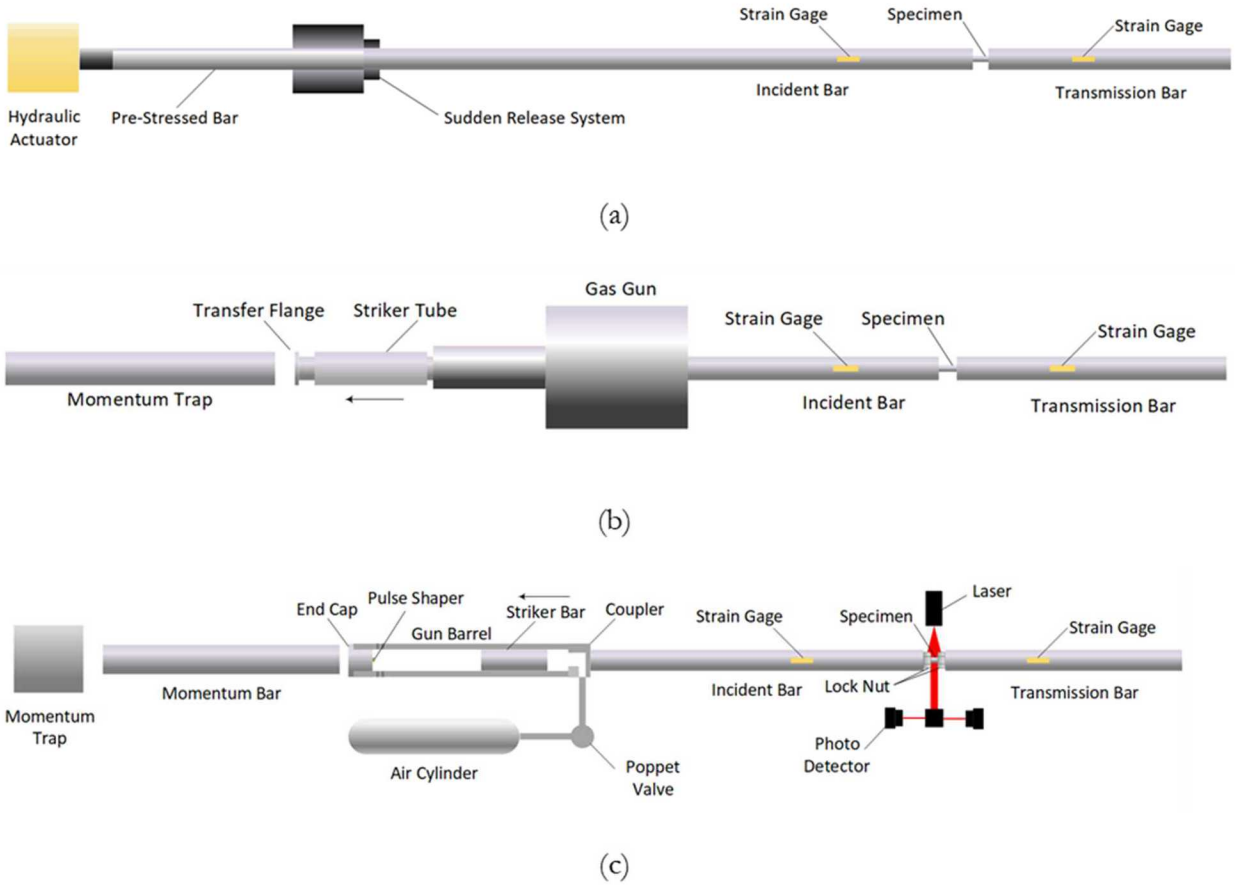

Figure 1.1. Schematics of different Kolsky tension bar designs

The pre-stretched Kolsky tension bar method uses stored elastic energy in a stretched section of the incident bar. A clamp divides the incident bar into two sections: pre-stressed and stress-free sections (as shown in Fig. 1.1(a)). Although different clamps have been designed by different research groups [39-43, 45-47], the overall principle of the clamp design is to release the stored elastic energy as quickly as possible. The release of the stored energy forms a tensile stress wave that propagates toward the specimen end of the incident bar. The amount of stored energy determines the amplitude of the tensile stress wave, while the length of the pre-stressed section determines the duration of the tensile stress wave. The pre-stretched Kolsky tension bar design can generate relatively long (~1 ms) tensile pulses [39, 42, 43, 45-47]. However, when the duration of the tensile pulse is longer than half of the length of the stress-free section in the incident bar, the tensile waves become overlapped requiring additional methods to separate the waves [39, 42, 43, 45, 86]. Dynamic stress equilibrium and constant strain rate are essential to achieve in Kolsky bar experiments and are usually accomplished through pulse shaping [18]. However, due to the nature of the clamp release method on the pre-stretched Kolsky tension bar (Figure 1.1(a)), pulse shaping is impossible to implement.

In the tubular striker Kolsky tension bar design, as shown in Fig. 1.1(b), a gas gun launches a tubular striker that impacts a flange on the incident bar. This method requires that the mechanical impedance be matched among the tubular striker, flange, and the incident bar to generate a nearly trapezoidal tensile pulse [66]. This design somewhat allows pulse shaping. Attaching a pulse shaper, or multiple pulse shapers to the impact flange changes the profile of the incident pulse to help the specimen achieve dynamic stress equilibrium and constant strain rate deformation [87, 88]. However, due to the

circular shape and relatively small contact area between the tubular striker and the flange, the design and installation of a pulse shaper is challenging and limited in effectiveness. The duration of the tensile pulse is also a concern with the tubular striker design. In general, the duration of the tensile pulse is determined by the length of the tubular striker, which is also limited by the length of the gas gun and incident bar that passes through the gas gun. Having the incident bar pass through the gas gun also limits the available strain gage positions along the incident bar. To circumvent the difficulties of the tubular striker and gas gun design, a modified method was recently developed that used a 2.5-m-long "U" shape striker or a 3-m-long tubular striker, driven by a pneumatic tube via an off-axis pull rod, to generate tensile pulses with a duration over 1 ms [89, 90]. Similarly, a long incident bar is needed to accommodate such a long pulse, or an additional wave-separation method must be used. Furthermore, this modification does not improve the limited possibilities of pulse shaping using the flange impact.

The most recent evolution in Kolsky tension bar design uses a solid striker (Fig. 1.1(c)) [77, 78]. The design by Sandia National Laboratories [78] is used here as an example to describe the solid striker technique. The whole Kolsky tension bar system is installed on an optical table to ease alignment. Like a previously developed Kolsky compression bar [90], both gun barrel and bars are supported and enclosed in pillow blocks with built-in Frelon-coated linear bearings to minimize friction. In this Kolsky tension bar design, the gun barrel is made of 4340 steel and serves as a portion of the loading train. The impact end of the gun barrel is enclosed by a threaded end cap while the opposite end is connected to the incident bar via a threaded coupler. The solid striker, which has the same diameter as the incident bar, is placed inside the gun barrel and is launched by the gas gun toward the end cap. The impact of the solid striker on the end cap generates a tensile stress wave in the gun barrel, which transmits into the incident bar. A pair of strain gages on the incident bar are used to measure the incident tensile stress wave (*incident wave*). When the incident wave arrives at the tensile specimen, part of it is reflected back in the incident bar as a *reflected wave,* and the rest transmits into the transmission bar as a *transmitted wave* measured with another pair of strain gages on the transmission bar, while the specimen is being elongated. This design enables direct application of pulse shaping to the Kolsky tension bar that is usually learned through Kolsky compression bar experiments [18]. Akin to placing a pulse shaper on the impact end of a Kolsky compression bar, a pulse shaper is placed on the inside surface of the end cap of the gun barrel before the endcap is threaded on the end of the gun barrel. Upon impact of the solid striker, the pulse shaper is compressed and can reach large deformation (as in the case of the compression bar). A well-shaped incident tensile pulse can be generated to minimize wave dispersion through physical low-pass filtering, achieve dynamic stress equilibrium in the sample by increased rise time, and attain constant strain rate deformation in the sample. In general, a trapezoidal pulse with a relatively long rise time (~100 μs) is sufficient to achieve these requirements, depending on the work hardening behavior of the material. Specimens possessing insignificant work hardening easily achieve constant strain rate when a trapezoidal pulse is applied. However, for materials with significant work-hardening behavior, such as Fe-49Co-2V alloy, an incident pulse with a distinct hardening slope, rather than a trapezoidal pulse is required. Fig. 1.2 shows typical incident pulses that are needed for Kolsky tension bar tests of metallic materials with insignificant and significant work hardening behavior. In special cases where the mechanical impedance of the tensile specimen with significant work-hardening is much smaller than (or negligible to) that of the bars, a trapezoidal incident pulse may be sufficient.

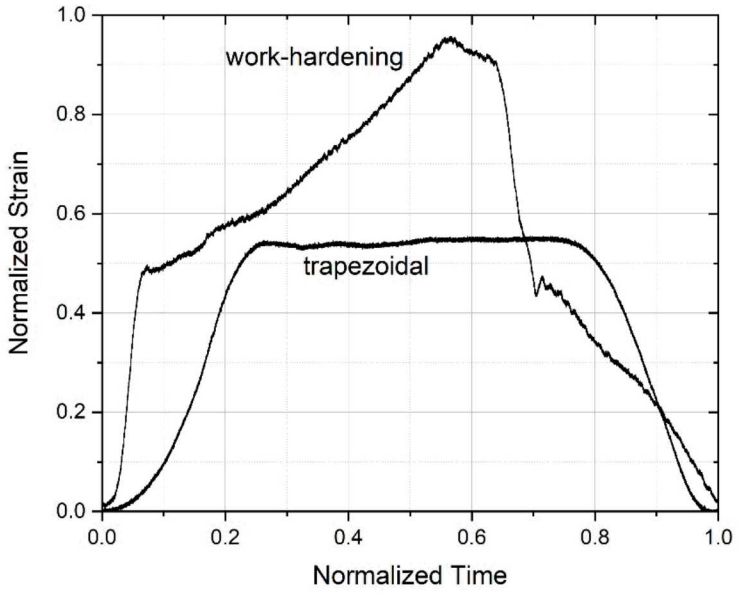

Figure 1.2. Incident pulses generated in Kolsky tension bar tests with a solid striker design

Because the gun barrel is a portion of the loading train, the mechanical impedance of the gun barrel ideally must match that of the striker and bars. However, this requirement may result in challenges in design and fabrication of the gun barrel. Another option in the design process is to eliminate the need for sabots on the striker. This can improve the alignment of the system as well as repeatability. If the inner diameter (ID) of the barrel is the same as the striker, the outer diameter (OD) needs to be precisely machined to satisfy

$$\rho_g C_g \left(A_o - A_i \right) = \rho_b C_b A_b \tag{1.1}$$

where ρ_g and C_g are density and elastic wave speed in the gun barrel material, respectively; ρ_b and C_g are density and elastic wave speed in the bar material, respectively; A_o and A_i are outside and inside cross-sectional areas of the gun barrel, respectively; A_b is the bar diameter, $A_b = A_i$. From Eq. (1.1), we have

$$A_o = \left(\frac{\rho_b C_b}{\rho_g C_g} + 1 \right) A_b \tag{1.2}$$

or

$$D_o^2 = \left(\frac{\rho_b C_b}{\rho_g C_g} + 1 \right) D_b^2 \tag{1.3}$$

where D_o and D_b are OD of the gun barrel and bar diameter, respectively. Therefore, the OD of the gun barrel is determined using

$$D_o = D_b \sqrt{\frac{\rho_b C_b}{\rho_g C_g} + 1} \tag{1.4}$$

If the gun barrel and bar are made of the same material, $\rho_g = \rho_b$, $C_g = C_b$, the OD of the gun barrel needs to be

$$D_o = \sqrt{2} \cdot D_b \tag{1.5}$$

In many cases, it may be desirable to design the gun barrel with relatively larger wall thickness to prevent plastic deformation, especially in threaded areas at the end cap and coupler. Such a design choice results in higher mechanical impedance compared to the bars and striker. When the propagating tensile stress wave arrives at the interface between the gun barrel and the incident bar, a portion of the tensile wave is reflected back into the gun barrel as a compression wave. This reflected compression wave is reflected again at the free end of the gun barrel in tension and then transmitted into the incident bar. This impedance-mismatched-induced wave may overlap with the reflected wave of the original incident wave at the incident bar/specimen interface, as illustrated in Fig. 1.3.

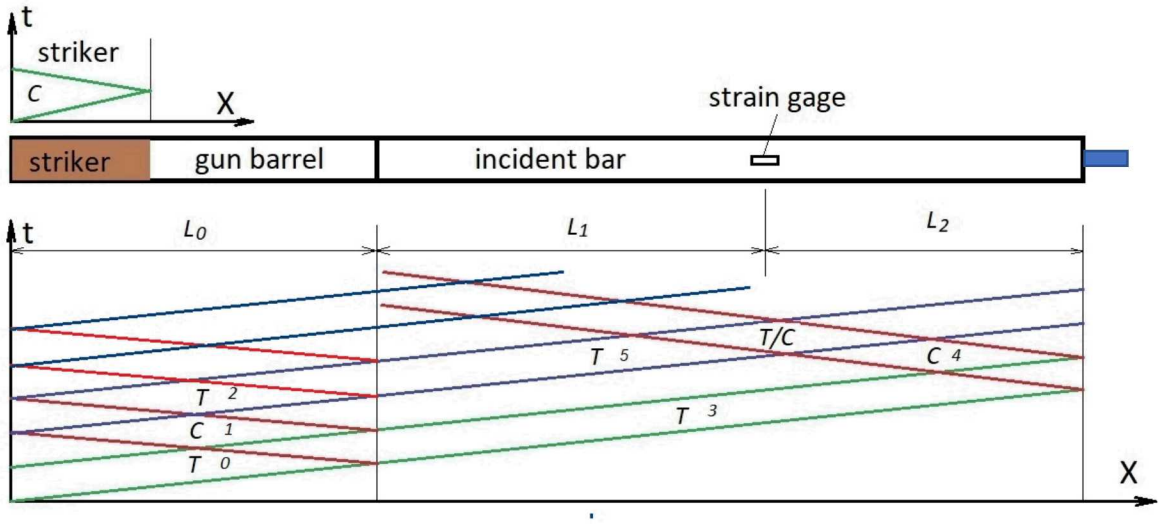

Figure 1.3. Stress wave propagation in the Kolsky tension bar

Here we consider the striker having the same mechanical impedance, $\rho_0 C_0 A_0$, as the incident bar, but lower mechanical impedance ($\rho_1 C_1 A_1$) than the gun barrel. If the tensile stress wave in the gun barrel generated by the impact of the striker is σ_{T0}, then the reflected compressive wave, σ_{C1}, and tensile wave transmitted into the incident bar, σ_{T3}, can be calculated with,

$$\sigma_{C1} = R \cdot \sigma_{T0} \tag{1.6}$$

$$\sigma_{T3} = T \cdot \sigma_{T0} \tag{1.7}$$

where the subscripts, T and C, represent tensile and compressive waves, respectively; $\bar{R}$ and $\bar{T}$ are reflection and transmission coefficients [91],

$$\bar{R} = \frac{1 - \dfrac{\rho_1 C_1 A_1}{\rho_0 C_0 A_0}}{1 + \dfrac{\rho_1 C_1 A_1}{\rho_0 C_0 A_0}} = \frac{\rho_0 C_0 A_0 - \rho_1 C_1 A_1}{\rho_0 C_0 A_0 + \rho_1 C_1 A_1} \tag{1.8}$$

$$\bar{T} = \frac{2}{1 + \dfrac{\rho_1 C_1 A_1}{\rho_0 C_0 A_0}} = \frac{2\rho_0 C_0 A_0}{\rho_0 C_0 A_0 + \rho_1 C_1 A_1} \tag{1.9}$$

When the reflected compressive wave (*C1*) in the gun barrel is reflected back again at the free end, the stress wave becomes a tensile wave (*T2*),

$$\sigma_{T2} = -\sigma_{C1} = -\bar{R} \cdot \sigma_{T0} \tag{1.10}$$

The tensile wave (*T2*) then transmits into the into the incident bar through the same gun barrel/incident bar interface,

$$\sigma_{T5} = \bar{T} \cdot \sigma_{T2} = -\bar{R} \cdot \bar{T} \cdot \sigma_{T0} \tag{1.11}$$

In the meantime, the tensile wave *T3* is reflected back as a compressive wave *C4* at the incident bar/specimen interface. Depending on the strain gage location, the arrival times for the tensile wave *T5* and the compressive wave *C4* to the strain gage location may be different, as illustrated in Fig. 1.4,

$$\Delta t = t_{T5} - t_{C4} = 2\left(\frac{L_0}{C_1} - \frac{L_2}{C_0}\right) \tag{1.12}$$

Note Δt could be positive if the compressive wave *C4* arrives earlier than the tensile wave *T5*, negative if the wave compressive *C4* arrives later than the tensile wave T5, or zero if both waves arrive at the same time. The actual signal that the strain gage measures is the result of overlapping of the tensile wave *T5* and compressive wave *C4*,

$$\sigma_{T/C}(t) = \sigma_{T5}(t + \Delta t) + \sigma_{C4}(t) \tag{1.13}$$

From Eq. (11), we have

$$\sigma_{T/C} = -\bar{R} \cdot \bar{T} \cdot \sigma_{T0} + \sigma_{C4} = -\bar{R} \cdot \sigma_{T3} + \sigma_{C4} \tag{1.14}$$

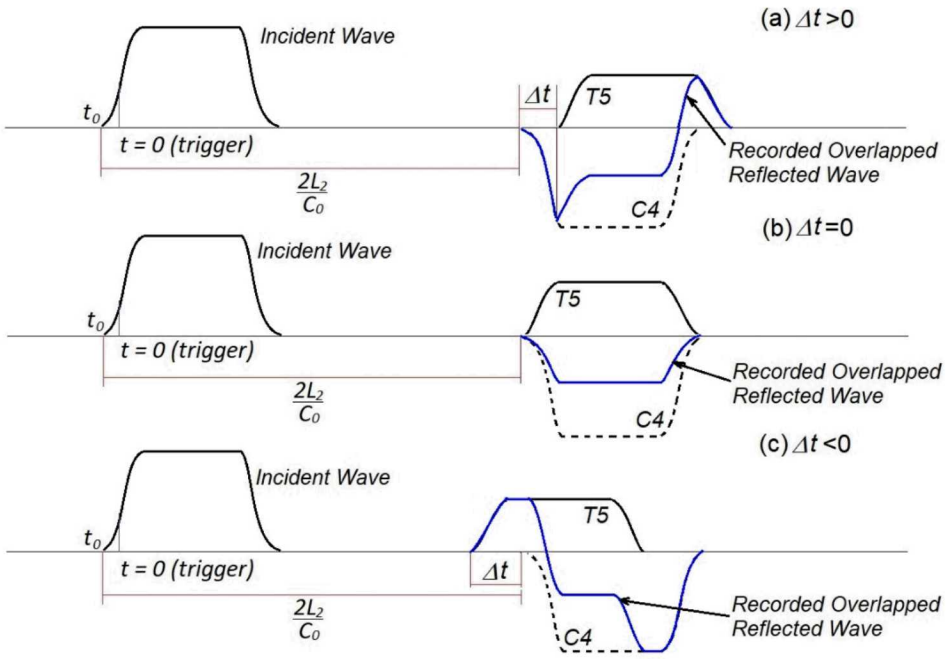

Figure 1.4. Illustration of stress wave overlapping

In Eq. (1.14), $\sigma_{T/C}$ represents the strain-gage-recorded overlapped reflected pulse where σ_{T3} is the incident pulse directly measured with the same strain gage. Therefore, the actual reflected wave at the incident bar/specimen interface is

$$\sigma_{C4} = \sigma_{T/C} + \overline{R} \cdot \sigma_{T3} \tag{1.15}$$

Considering a total duration of loading, T_0, determined by the striker length, L_{striker}, with an elastic wave speed, C_{striker},

$$T_0 = 2 \cdot \frac{L_{\text{striker}}}{C_{\text{striker}}} \tag{1.16}$$

no overlapping occurs if $|\Delta t| > T_0$. However, it is preferred that $\Delta t > T_0$,

$$L_2 < C_b \cdot \left(\frac{L_0}{C_g} - \frac{L_{\text{striker}}}{C_{\text{striker}}} \right) \tag{1.17}$$

In addition, L_2 needs to be longer than L_{striker} to avoid the overlapping between the incident tensile wave *T3* and the reflected compression wave *C4*. Therefore, to avoid wave overlapping, the strain gage location needs to be

$$L_{\text{striker}} < L_2 < C_b \cdot \left(\frac{L_0}{C_g} - \frac{L_{\text{striker}}}{C_{\text{striker}}} \right) \tag{1.18}$$

If the striker and the incident bar are made of the same material, $C_{\text{striker}} = C_b$, Eq. (18) becomes

$$L_{\text{striker}} < L_2 < \frac{C_b}{C_g} \cdot L_0 - L_{\text{striker}} \tag{1.19}$$

If the gun barrel material has the same elastic wave speed as the incident bar material, $C_g = C_b$, Eq. (1.19) can be further simplified as

$$L_{\text{striker}} < L_2 < L_0 - L_{\text{striker}} \tag{1.20}$$

Eq. (1.20) also requires

$$L_{\text{striker}} < \frac{1}{2} L_0 \tag{1.21}$$

Eq. (21) suggests that the striker needs to be shorter than half of the length of the gun barrel to avoid the reflected wave being overlapped.

When the strain gage location does not satisfy Eq. (1.18), the reflected compression wave is overlapped but can be reconstructed with Eq. (1.15).

With assumption of stress equilibrium, the reflected wave (ε_r) can be calculated with the incident (ε_i) and transmitted waves (ε_t),

$$\varepsilon_r = -\varepsilon_i + \varepsilon_t \tag{1.22}$$

The classical calculations of specimen strain rate, strain, and stress,

$$\dot{\varepsilon} = \frac{C_b}{L_s} \cdot \left(\varepsilon_i - \varepsilon_r - \varepsilon_t \right) \tag{1.23}$$

$$\varepsilon = \frac{C_b}{L_s} \cdot \int_0^t \left(\varepsilon_i - \varepsilon_r - \varepsilon_t \right) dt \tag{1.24}$$

$$\sigma = E_b \cdot \left(\varepsilon_i + \varepsilon_r + \varepsilon_t \right) \cdot \frac{A_b}{2A_s} \tag{1.25}$$

can be rewritten as

$$\dot{\varepsilon} = -2 \cdot \frac{C_b}{L_s} \cdot \varepsilon_r = 2 \cdot \frac{C_b}{L_s} \cdot \left(\varepsilon_i - \varepsilon_t \right) \tag{1.26}$$

$$\varepsilon = -2 \cdot \frac{C_b}{L_s} \cdot \int_0^t \varepsilon_r dt = 2 \cdot \frac{C_b}{L_s} \cdot \int_0^t \left(\varepsilon_i - \varepsilon_t \right) dt \tag{1.27}$$

$$\sigma = E_b \cdot \varepsilon_t \cdot \frac{A_b}{A_s} \tag{1.28}$$

where E_b is Young's modulus of the bar material; L_s and A_s are specimen gage length and cross-sectional area, respectively.

Dynamic Tensile Specimen Design and Mounting Method

Metallic specimen design for dynamic tensile tests depends on the product form and nature of material behavior. In general, Kolsky tension bar specimens must be in either cylindrical or sheet form. Each form requires different mounting methods. Regardless of form, the gage length of tensile specimens must be designed based on the desired maximum strain and/or strain rate applied to the specimen. There is a limit on the maximum impact velocity and duration that can be applied with a Kolsky tension bar, which also imposes a limit on maximum displacement. At the limit of impact velocity and displacement of a certain system, a shorter gage length yields a higher strain rate and maximum strain.

1. Cylindrical Specimen

Cylindrical specimen with a "dog-bone" shape is the most common form in Kolsky tension bar tests of metallic materials. In design of such a "dog-bone" cylindrical specimen, two parameters–gage length (L_s) and aspect ratio (length-to-diameter ratio, L_s/D_s)–must be seriously considered. The conventional ASTM standard [92] for quasi-static tensile tests is generally not applicable for Kolsky tension bar tests due to the essential requirement of dynamic stress equilibrium. In order to generate relatively equilibrated stress, the specimen needs to be sufficiently short such that stress waves can "ring" back and forth to achieve a uniform stress state inside the specimen within a short period of time. However, a relatively large aspect ratio (L_s/D_s) is needed to generate approximate uniaxial stress state in the gage section. Staab and Gilat [39] varied specimen geometries to optimize the tensile specimen length-to-diameter ratio for Kolsky tension bar tests. They concluded that the L_s/D_s needs to be 1.6 or greater. Smaller L_s/D_s produced a higher flow stress due to a stress-state with increased triaxiality. With a combined experimental-numerical approach, Godinger et al. [93] drew similar conclusions that the aspect ratio, also defined as "wavelength," significantly affected the growth rate of necking. The growth rate of the neck increased non-linearly with increasing aspect ratio (or "wavelength") and eventually saturated [93]. Fig. 5 summarizes the cylindrical tensile specimen geometry designs from different research groups. Although different gage lengths and aspect ratios have been used by different groups, the geometry with a gage length between 5 and 10 mm and an aspect ratio between 1.5 and 2 has been utilized most often, as circled in Fig. 1.5,

$$5\ mm \le L_s \le 10\ mm \tag{1.29}$$

$$1.5 \le \frac{L_s}{D_s} \le 2.0 \tag{1.30}$$

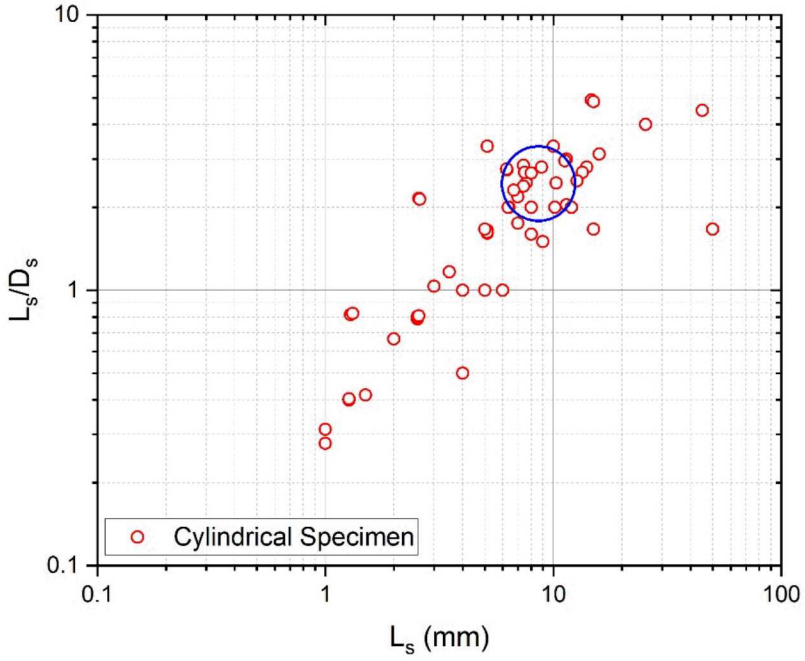

Figure 1.5. Cylindrical tensile specimen design

Cylindrical "dog-bone" specimen designs also require a transitional radius or shoulder between the gage section and larger-diameter threaded ends are needed to attach the specimen to the tension bars. The radius design must be carefully considered and has not received much attention in the literature. A small radius may increase the stress concentration and consequently result in premature failure within the transitional region. Conversely, a large radius increases the overall length of the specimen, which extends the time required to achieve stress equilibrium. Furthermore, when the overall displacement is used to calculate the specimen strain over the gage section the deformation within the transitional region must also be considered depending on the strain measurement method. Without proper correction, the specimen strain over the gage section would be overestimated. A larger radius generates a more significant underestimation of specimen strain over the gage section, which will be presented later. Fig. 1.6 shows an example of the cylindrical tensile specimen design with a nominal gage length of 6.35 mm and a L_s/D_s of 2, which has been used at Sandia National Laboratories.

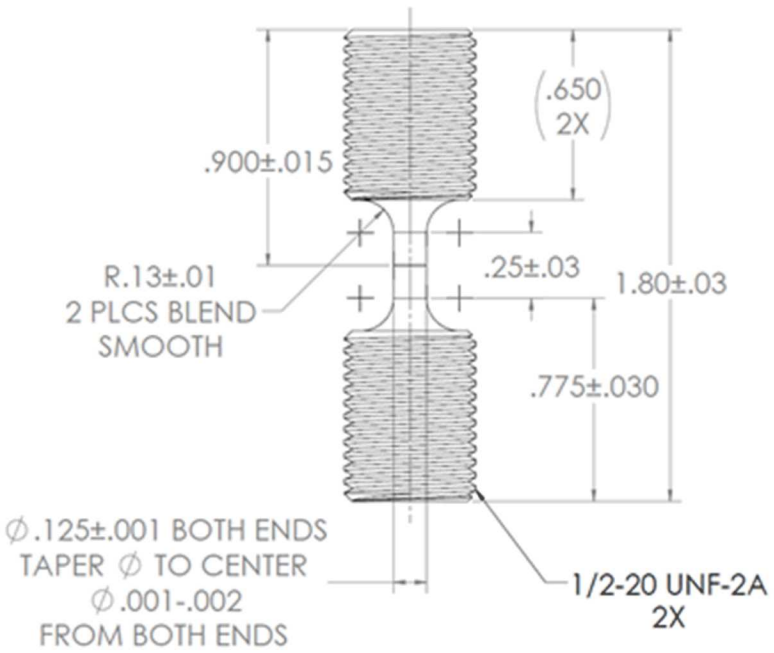

Figure 1.6. An example of cylindrical tensile specimen design-dimensions in inches

A general practice to mount a cylindrical tensile specimen is to directly thread the specimen into the bar ends. However, imperfect contact between the threads may result in a significant pseudo stress peak that overshadows the intrinsic yield strength of the specimen material [94]. Recently, a pair of lock nuts (shown in Fig. 1.7(a)) have been shown to improve the contact between the threads and effectively minimize the pseudo stress peak. Fig. 1.7(b) shows a comparison of specimen stress histories with and without lock nuts applied, under the same loading conditions [95]. Without the lock nuts, significant oscillations in the specimen stress history were observed due to interfacial impact between the threads. In addition, the stress initiation was significantly delayed in the case without lock nuts, indicating that approximately 60 μs was required for the threads to fully engage. When the lock nuts were applied, the thread engagement was improved such that the stress oscillations disappeared. The lock nut method also prevented any torque from being applied to the gage section of the specimen during the installation process since torque is applied to the lock nuts and bar individually. The torque applied to the lock nuts can be varied to minimize the stress wave disturbance as the wave propagates through the threads. This has been shown to make the reflected pulse more reliable for specimen strain rate and strain calculation with conventional Kolsky bar data reduction processes [96]. The lock nut torque required to minimize the stress wave disturbance may be different depending on the specimen material.

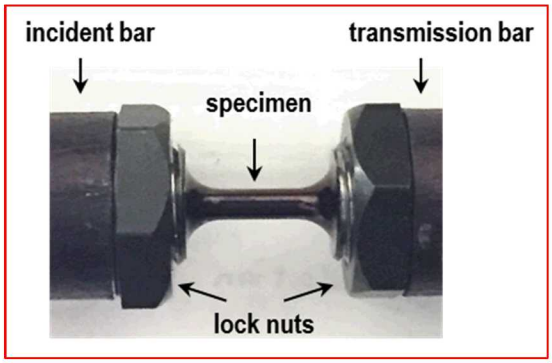

(a)

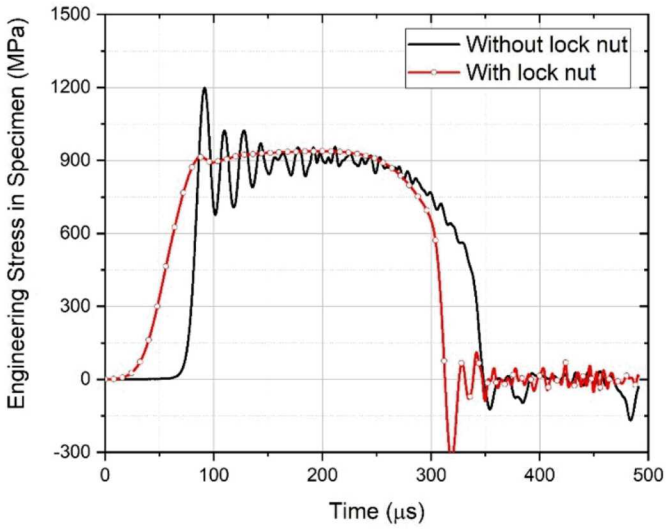

(b)

Figure 1.7. Lock nut application (a) and effect on specimen stress history (b) [84]

2. Sheet Specimen

When the material under investigation comes in sheet metal form, the specimen design is a flat "dog-bone" shape with a pre-determined thickness, as shown in Fig. 1.8. Similar to the cylindrical dog-bone specimens, the gage length (L_s) and length-to-width ratio (L_s/W_s) become critical to the design. Rusinek et al. [97-99] investigated "dog-bone" sheet specimens with different gage length and length-to-width ratios for Kolsky tension bar tests and recommended a gage length of less than 10 mm to achieve dynamic equilibrium.

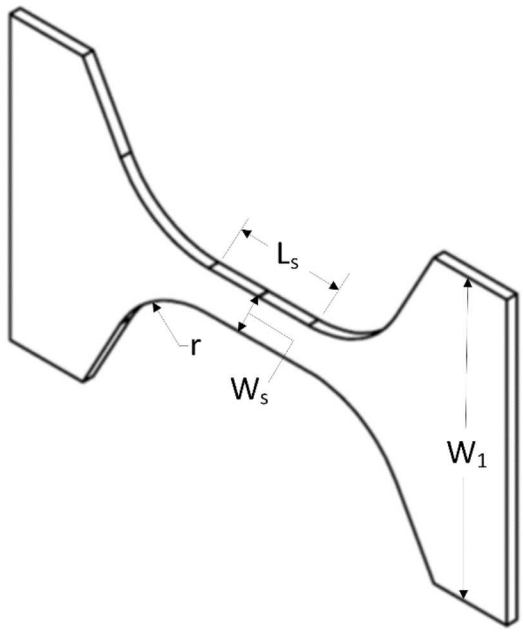

Figure 1.8. Schematic of sheet tensile specimen design

Fig. 1.9 shows the range of sheet "dog-bone" specimen designs in terms of gage length and length-to-width ratio used in different studies. Although various specimen designs were investigated, a narrow range was identified and is circled in Fig. 1.9, where the optimal L_s and L_s/W_s were

$$5\ mm \le L_s \le 10\ mm \tag{1.31}$$

$$1.5 \le \frac{L_s}{W_s} \le 2.0 \tag{1.32}$$

The width (W_1) of the ends of the sheet "dog-bone" specimen and transitional radius, r, have also been discovered to affect the stress distribution in the specimen ends [99]. A large width ratio between the specimen end and gage section (W_1/W_s) and transitional radius were recommended to minimize effects of specimen end deformation, where $W_1/W_s = 3$, $r = 10\ mm$.

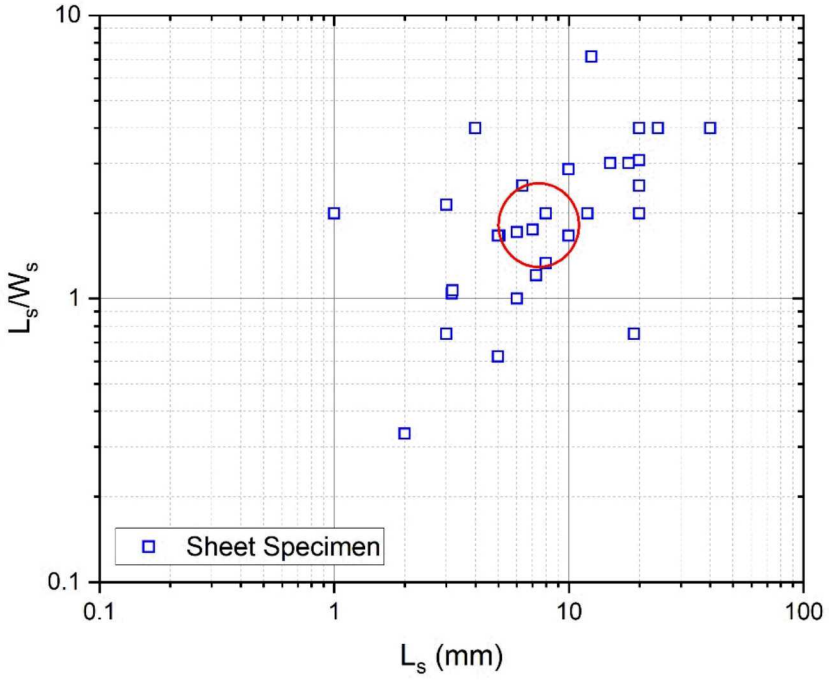

Figure 1.9. Sheet tensile specimen designs

When the sheet material is brittle, such as tungsten, the gage section may need to be tapered, but not too aggressively, to ensure failure within the gage section. Sanborn et al. [100] investigated tapered specimen designs for dynamic tensile experiments on pure tungsten and discovered an optimal width reduction of 0.36 mm compared to a non-tapered gage section for this material, as shown in Fig. 1.10. When the taper was too small (0.25 mm) (Fig. 1.11(a)), or too large (0.46 mm) (Fig. 1.11(c)), the specimen failed outside the gage section. With a taper of 0.36 mm however, the specimen consistently failed within the gage section (Fig. 1.11(b)).

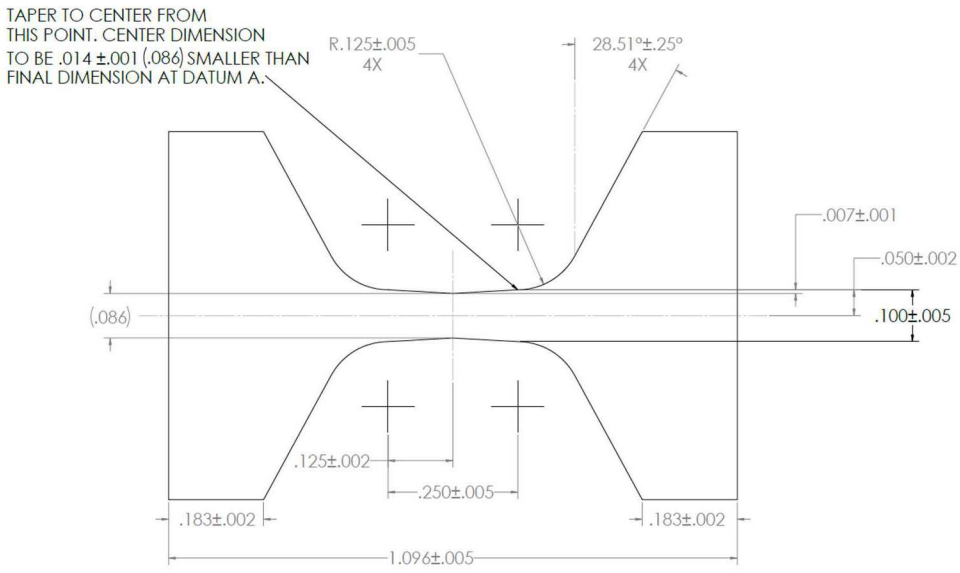

Figure 1.10. A tapered tensile specimen design—dimensions in inches [100]

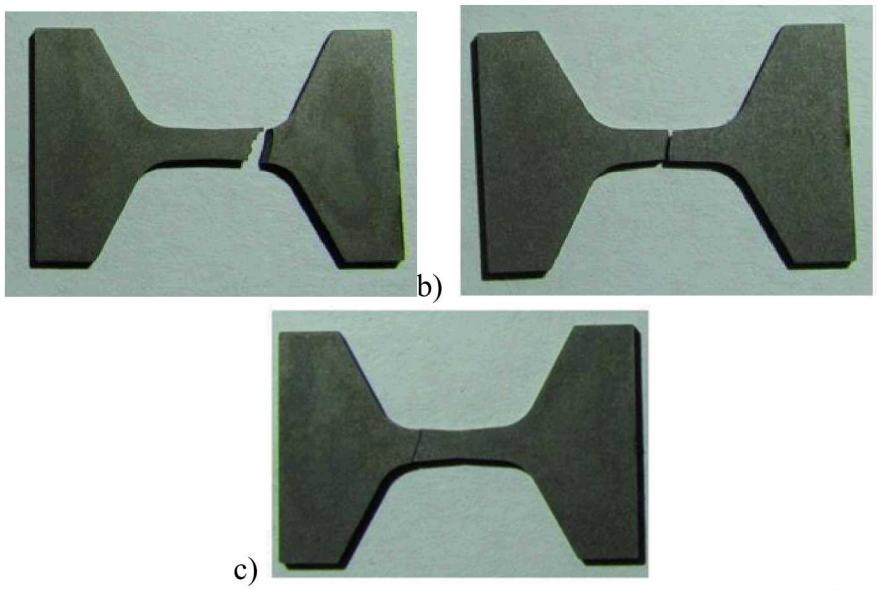

Figure 1.11. Comparison of fracture location of tungsten sheet tensile specimen with different taper sizes: 0.25 mm (a), 0.36 mm (b), and 0.46 mm (c) [100].

Unlike cylindrical specimen design (Fig. 1.6), gripping the sheet "dog-bone" specimen is more complicated. Four primary gripping methods have been used for Kolsky tension bar tests of sheet specimens: adhesively bonded mounting, clamping, dowel-pin mounting, and form-fit mounting, as illustrated in Fig. 1.12 [57, 76, 101].

Adhesively bonded mounting (Fig. 1.12(a)) is straightforward but requires the use of high shear strength adhesive such that

$$\tau \cdot A_1 > \frac{1}{2} \cdot \sigma_m \cdot W_s \cdot h_0 \tag{1.33}$$

where τ is the shear strength of the adhesive, A_1 is the adhesive contact area, σ_m is the maximum tensile strength of the specimen material, and h_0 is the thickness of the specimen. The adhesive contact area, A_1, needs to be

$$A_1 > \frac{\sigma_m \cdot W_s \cdot h_0}{2 \cdot \tau} \tag{1.34}$$

For a certain specimen design, the shear strength of adhesive, τ, needs to be

$$\tau > \frac{\sigma_m \cdot W_s \cdot h_0}{2 \cdot A_1} \tag{1.35}$$

Depending on the adhesive, a long cure time may be required prior to testing and can take significant effort to remove the adhesive after dynamic tests. In their study, Ledford et al. [57] used Loctite EA 9514, which had a shear strength of 50 MPa and cure time of 1 hour at 150ºC to reduce the needed time.

Mechanical clamping methods (Fig. 1.12(b)) employ a bolt to apply a normal force, F_N, to the sheet specimen such that the friction between the clamps and the specimen is sufficient to grip the specimen during dynamic tensile tests [101, 102],

$$F_N \geq \frac{\sigma_m \cdot W_s \cdot h_0}{\mu} \tag{1.36}$$

where μ is friction coefficient between the clamp and specimen materials. When subjected to axial tension, the specimen can potentially slip due to partially reduced clamping force during the test. Therefore, the bolt needs to be initially stretched to compensate for the potential loss of the clamping force during the test. The preload of the bolt is critical and must be carefully determined to provide adequate clamping force throughout the entire test. The required preload may also change depending on the material and loading conditions.

Dowel-pin mounting (Fig. 1.13(c)) allows for the quickest turnaround between experiments but has a few special considerations [102]. Specimens are designed with two mounting holes on each end of the tensile specimen. The specimen is placed in special grips threaded into the bar ends, which have dowel pins to hold the specimen. The tensile load is transferred to the specimen via shear through the dowel pins. The shear strength of the dowel pins must be larger than the load required to fail the tensile specimen. The specimen must be designed with enough material to prevent deformation and failure at the pin hole due to stress concentrations. The tolerance of the pin and hole may also affect the data quality in such Kolsky tension bar tests. Because the material between the pin hole and the gage section is subjected to tensile deformation, care must be taken to measure and calculate the specimen strain over the gage section.

Form-fit mounting (Fig. 1.14(d)) transfers the load in the specimen gage section through a shoulder and precisely matched mounting fixture. The tapered ends of the specimen are placed in the slot of the mounting fixture and secured with a cap [77, 81]. Stress concentrations may be created in the shoulder region during loading. Therefore, the design becomes critical and may require finite element simulation to optimize the geometry [58].

Through comparison of the adhesively bonded, dowel-pin, and form-fit mounting methods for sheet specimens, Ledford et al. [57] concluded that form-fit mounting provided the best result because significant oscillations were generated in the other two methods.

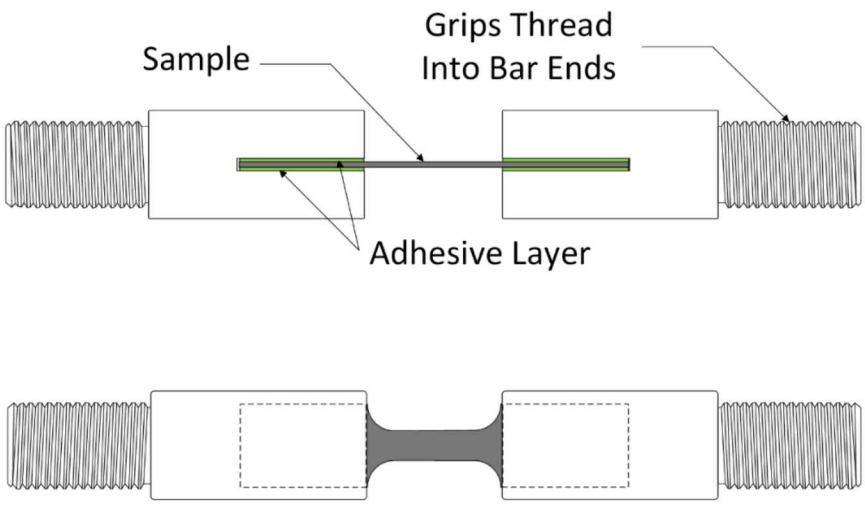
Grips Thread
Into Bar Ends
Sample
Adhesive Layer

(a)

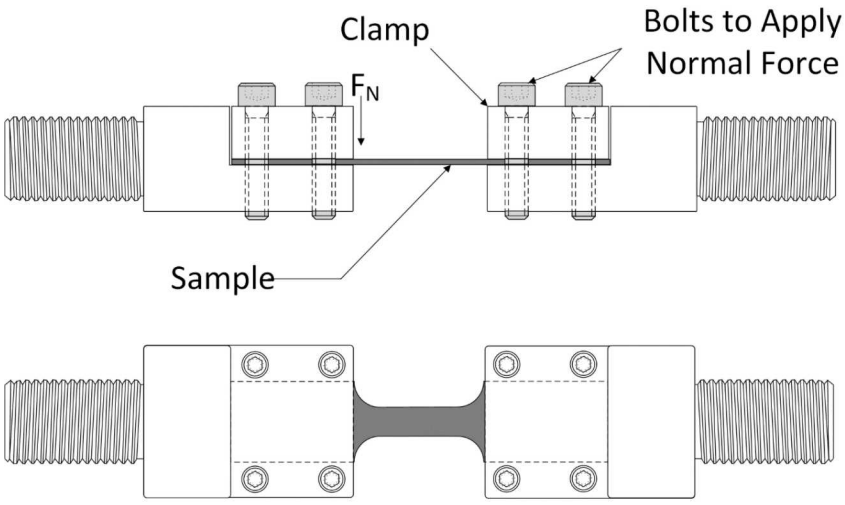
Clamp
Bolts to Apply
Normal Force
F_N
Sample

(b)

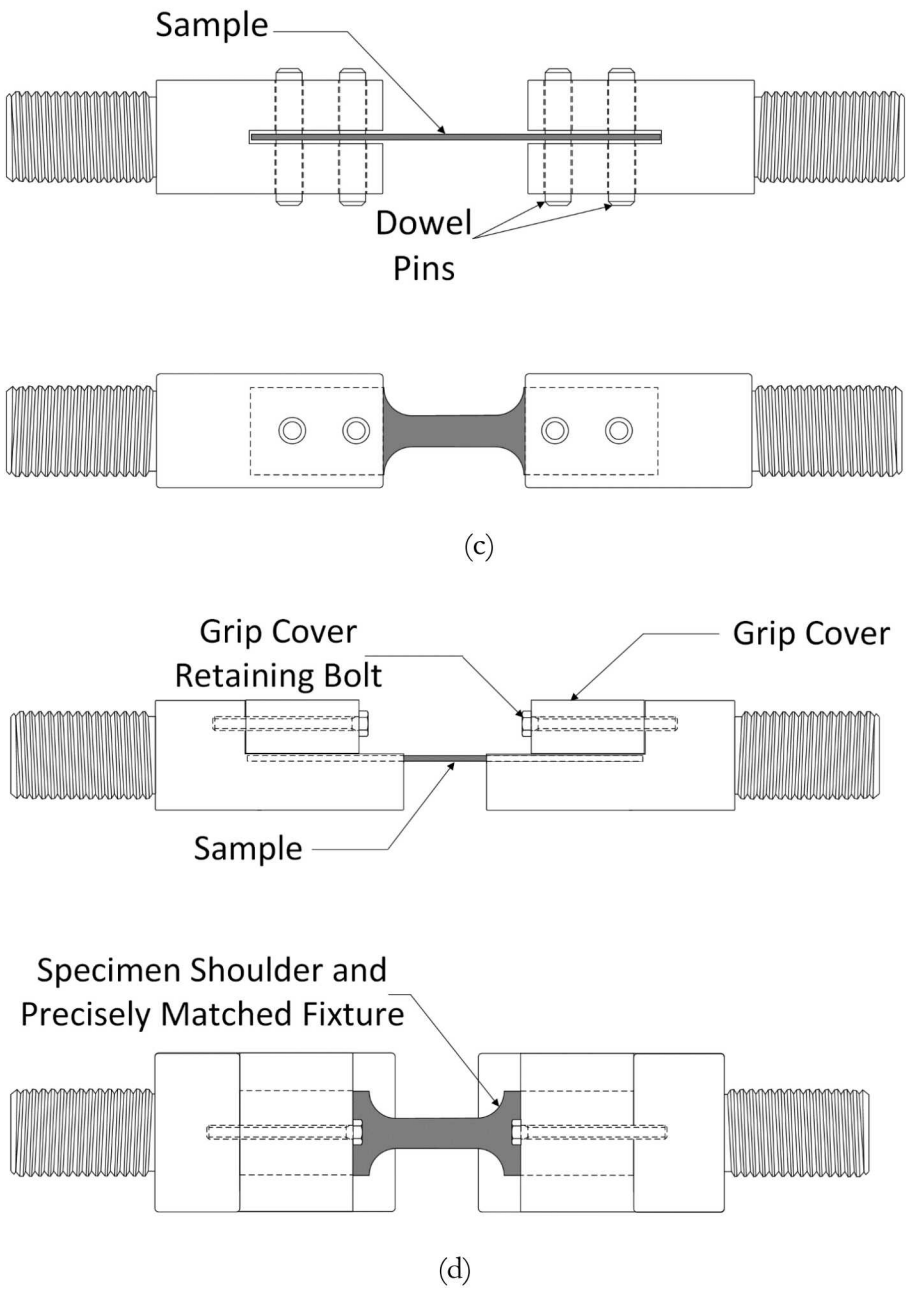

Figure 1.12. Illustration of sheet specimen mounting methods [101, 102]. a) adhesively bonded mounting, b) mechanical clamping mounting, c) dowel pin mounting, d) form fit mounting

Specimen Strain Measurement and Correction

Experimental Measurements

In a Kolsky tension bar test, the specimen stress calculation is straightforward with Eq. (1.25) or (1.28), whereas the specimen strain calculation must be handled carefully due to the specimen geometry. Specimen strain is generally calculated using displacements at the front (L_f) and back (L_b) end of the specimen obtained from the incident, reflected, and transmitted pulses from bar strain gages,

$$L_f = C_b \cdot \int_0^t (\varepsilon_i - \varepsilon_r) dt \tag{37}$$

$$L_b = C_b \cdot \int_0^t \varepsilon_t dt \tag{38}$$

The specimen displacement is thus

$$\Delta L = L_f - L_b = C_b \cdot \int_0^t (\varepsilon_i - \varepsilon_r - \varepsilon_t) dt \tag{39}$$

As mentioned earlier, the threads may disturb stress wave propagation, which makes the reflected pulse unreliable except when lock nuts are used with specific pre-torque [95]. As an alternative method, a high-speed laser extensometer has been developed to directly and independently measure the displacements at both ends of the specimen [95, 103], as shown in Fig. 1.13. A collimated sheet laser generated by an integrated line laser and convex lens is positioned across the gap between the incident and transmission bar. The width of the sheet laser is precisely adjusted to accommodate the entire gage section and transitional sections (shoulders) of the specimen. A right-angle prism mirror, to which the apex was aligned in the optical axis, splits the sheet laser into two independent beams corresponding to incident and transmission bar motion. The transmission bar side beam is focused to a point and collected using a single high-speed photodetector. The incident bar side beam is further separated by a pellicle beam splitter and focused into two additional photodetectors to instantaneously measure the incident bar displacement at two different levels of resolution. The high-resolution channel (amplified channel) is dedicated to measuring the initial small displacement of the specimen. However, the signal becomes saturated when the displacement at the incident bar end becomes large. The low-resolution channel records the displacement signal for the entire loading duration. In some cases, a single channel may be enough to cover the entire displacement with sufficient resolution [103]. The transmission bar side was recorded with a similarly amplified channel because the displacement on the transmission bar side is usually much smaller than the incident bar side. The custom laser extensometer must be carefully calibrated prior to dynamic tensile tests by simulating the bar-end motion using a micrometer-equipped translation stage. The laser extensometer showed high resolution and acceptable linearity for not only dynamic tensile tests, but also dynamic compression tests with a Kolsky compression bar [104].

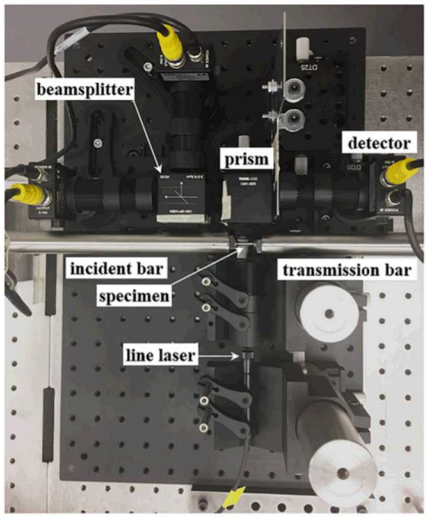

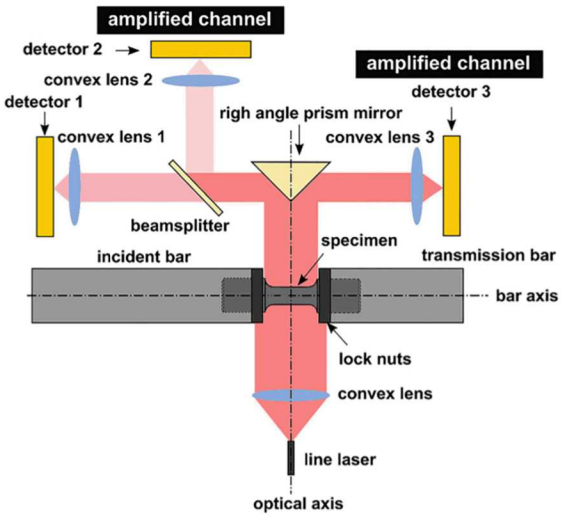

Figure 1.13. High-speed laser extensometer.

Displacement measurements made with either the bar strain gages, or the high-speed laser extensometer represent the displacement of not only the specimen gage section, but also the non-gage section, i.e., the shoulder. Using the specimen gage length with the raw displacement to calculate strain results in overestimation, whereas if the length including the shoulder is used, the strain is underestimated, as is discussed in the following section. Therefore, direct measurement of specimen strain is desirable to avoid concerns of over or underestimation.

Direct strain measurements are typically made with either contact or non-contact methods. The primary contact strain measurement method is to attach a miniature strain gage directly to the gage section of the specimen. However, the measurement range of most strain gages is limited to approximately 5% strain, which narrows the application to brittle, rather than ductile metallic materials [62, 105]. High-speed imaging has recently emerged as the primary method to make non-contact direct strain measurements. In terms of strain quantification, high-speed line or point tracking over the gage length is a straightforward and relatively simple method that has been used extensively to investigate dynamic fracture of metallic materials during Kolsky tension bar tests [44, 46, 61, 70, 85, 90]. In this method, two parallel lines are painted or drawn within the specimen gage section that is imaged with a high-speed camera or a fast line scan camera to track the movement of the two lines independently. The relative displacement between the two lines gives the specimen displacement over the gage section and the specimen strain is thus calculated. This method provides an average displacement or strain measurement between the two lines over the gage section. Although a transient optical method based on digital speckle correlation method (DSCM) was developed [106], high-speed digital image correlation (DIC) has been broadly applied to provide full-field displacement and deformation information of the specimen surface during dynamic tests [23, 50, 64, 75, 107-109]. X-ray DIC (XDIC) has also been developed for internal high-rate specimen deformation measurement [71]. A benefit of DIC over other methods is that it provides both average and local measurements of specimen strain. With DIC, a random speckle pattern is painted on the specimen surface prior to dynamic tests. A high-speed digital camera is employed to photograph the pattern during deformation of the specimen. Displacements and strain fields are calculated by tracking the pixel intensity or gray-scale value over a set of images. Though DIC is popular due to ease of implementation and the ample data that it provides, some practical experimental concerns exist. The survivability of the paint during dynamic tensile tests is a primary concern when using the DIC method, particularly for high-ductility materials. The spatial and temporal resolution of the high-speed camera may also limit the resolution of the resulting specimen deformation measurement.

Another, simpler high-speed imaging technique for strain measurement is to use a high-speed camera to track the change of cross-section area of the tensile specimen,

$$\varepsilon_{true} = \ln\left(\frac{A_s}{A}\right) \tag{1.40}$$

where ε_{true} is true strain, A is instantaneous specimen cross-sectional area during dynamic tension, A_s is the initial cross-sectional area of the tensile specimen. For an isotropic cylindrical specimen, Eq. (1.40) becomes [51]

$$\varepsilon_{true} = 2\ln\left(\frac{D_s}{D}\right) \tag{1.41}$$

where D is instantaneous specimen diameter measured from the high-speed images. The true stress is directly calculated with

$$\sigma_{true} = E_b \cdot \left(\frac{D_b}{D} \right)^2 \cdot \varepsilon_t \tag{1.42}$$

For a sheet specimen, Eq. (1.40) is rewritten as

$$\varepsilon_{true} = \ln\left(\frac{W_s \cdot h_0}{W \cdot h} \right) \tag{1.43}$$

where W and h are instantaneous width and thickness of the sheet tensile specimen, respectively. Therefore, two synchronized high-speed cameras are needed to track the specimen width and thickness simultaneously.

Rather than high-speed imaging, a simple laser occlusive radius detector (LORD) was developed to directly measure the local diametral strain [48, 110]. The LORD and the laser extensometer mentioned earlier are both based on the same principal, but the LORD is positioned perpendicular to the axis of the tensile specimen and loading direction. Because the LORD technique relates the specimen diameter to the change in laser intensity, only cylindrical isotropic specimens may be used. Effectively implementing the LORD method to measure the full stress-strain behavior of a material may be challenging due the need to measure the precise minimum diameter of the neck, especially in ductile metals. Though altering the specimen design to encourage neck formation in a certain spot is possible, the final position of the neck within the gage section is not always known. Furthermore, the entire specimen may displace during deformation resulting in diameter measurements of different points over the gage section. Therefore, the LORD method may only be accurate up to the onset of necking for Kolsky tension tests on metals.

Numerical Correction for Cylindrical Specimens

Using either the conventional bar-strain-gages or the high-speed laser extensometer is the simplest way to obtain the specimen displacement. However, as mentioned previously, both measurements include the displacements of both gage section and shoulder. Deformation of the shoulder complicates the strain calculation because the shoulder may be partially subjected to plastic deformation for work-hardening materials. A numerical method to correct the specimen strain over the gage section has been developed for cylindrical specimens and is illustrated in Fig. 1.14 [111].

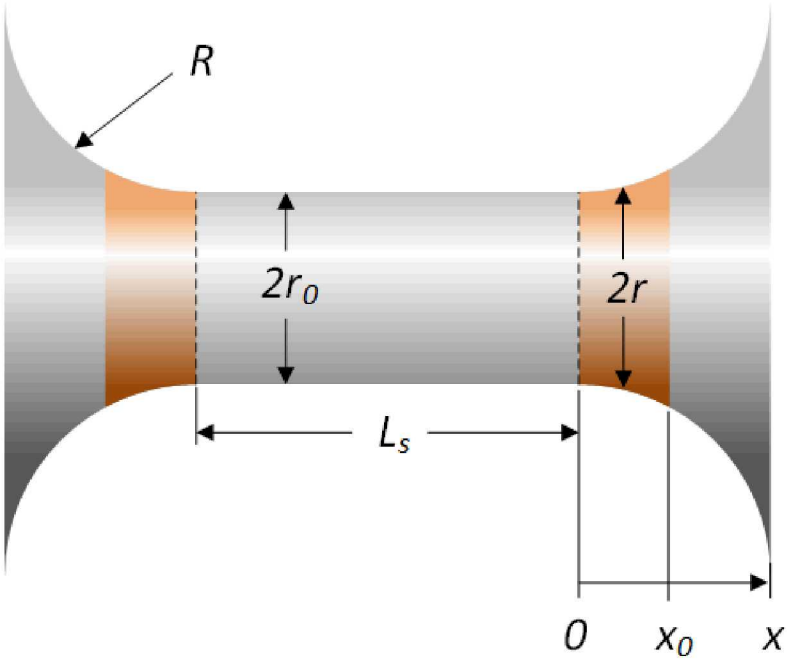

Figure 1.14. Illustration of gage and non-gage (shoulder) sections of a cylindrical tensile specimen.

In the correction analysis, the stress-strain response was divided into the following four regions, as illustrated in Fig. 1.15, where σ_{y1} and σ_{y2} are upper and lower yield strengths, respectively; σ_{ult} is the ultimate tensile strength; F_{y1} , F_{y2} , and F_{ult} are corresponding forces at upper yield, lower yield, and onset of necking. The following describes the regions.

Region I: elastic region over the gage section, when $\sigma < \sigma_{y1}$. In this region, the non-gage sections are also in elasticity.

Region II: post-yield region over the gage section, when $\sigma_{y2} < \sigma < \sigma_{y1}$. In this region, the gage section is in early plasticity while the non-gage sections remain in elasticity.

Region III: large plastic region over the gage section, when $\sigma > \sigma_{y1}$. In this region, the gage section is in large plastic deformation and portions of the non-gage sections plastically deform due to increased force (work-hardening).

Region IV: necking region in the gage section, when $\varepsilon > \varepsilon_{ult}$. In this region, the deformation over the gage section is highly localized due to necking. The non-gage sections are subjected to elastic recovery (unloading) because the applied force drops.

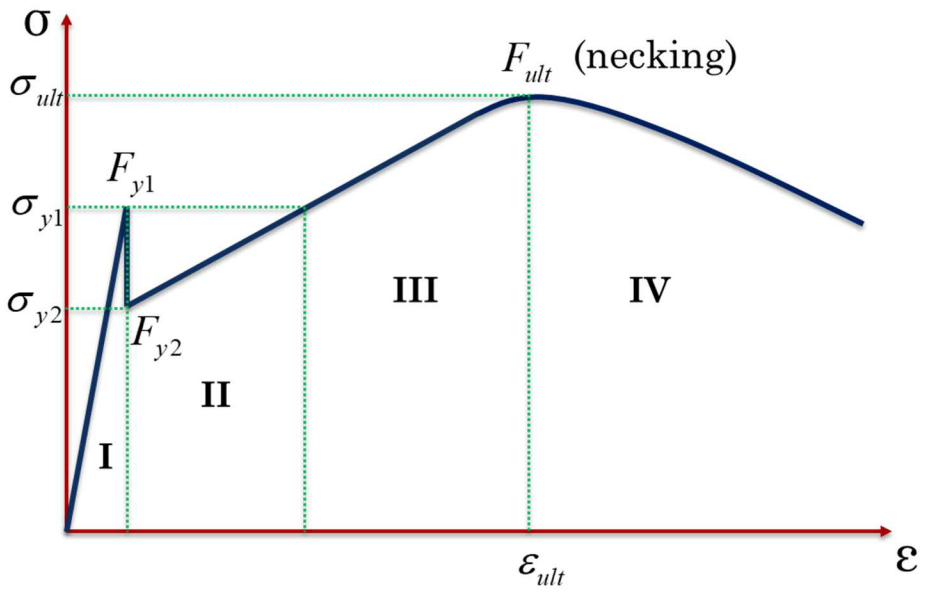

Figure 1.15. Idealization of a linear elastic, work-hardening stress-strain response with high/low yields and necking [111]

After the total specimen displacement (ΔL) is measured with the laser extensometer system or the bar-strain-gage method (Eq. (1.39)) and the specimen force history is determined with the transmitted bar strain signal, the specimen strain over the gage section can be determined with

$$\varepsilon = \begin{cases} c' \cdot \dfrac{\Delta L}{L_s} & \text{(Region I)} \\ \dfrac{\Delta L}{L_s} - \dfrac{F}{E_s \cdot \pi \cdot r_0^2} \cdot \left(\dfrac{1}{c'} - 1 \right) & \text{(Region II)} \\ \dfrac{F_{y1}}{E_s \cdot \pi \cdot r_0^2} + \dfrac{\Delta L - \dfrac{2 \cdot F}{E_s \cdot \pi} \cdot \int_{x_0}^{x_l} \dfrac{dx}{\left(R + r_0 - \sqrt{R^2 - x^2} \right)^2} - \dfrac{F_{y1}}{E_s \cdot \pi \cdot r_0^2} \cdot (2x_0 + L_s)}{\dfrac{2 \cdot F \cdot r_0^2 \cdot \int_0^{x_0} \dfrac{dx}{\left(R + r_0 - \sqrt{R^2 - x^2} \right)^2} - 2 \cdot F_{y2} \cdot x_0}{F - F_{y2}} + L_s} & \text{(Region III)} \\ \varepsilon\big|_{F=F_{ult}} + \dfrac{\Delta L - \Delta L\big|_{F=F_{ult}}}{L_s} + \dfrac{F_{ult} - F}{E_s \cdot \pi \cdot r_0^2} \cdot \left(\dfrac{1}{c'} - 1 \right) & \text{(Region IV)} \end{cases} \tag{1.44}$$

where x_0 represents the plastic region in the non-gage section, the boundary of which moves toward the specimen ends with increasing dynamic tensile force; c' represents the specimen strain correction factor for the linear elastic portion, which directly influences the determination of modulus of elasticity,

$$x_0 = r_0\sqrt{\left(\sqrt{\frac{F}{F_{y1}}}-1\right)\cdot\left[2\cdot\frac{R}{r_0}-\left(\sqrt{\frac{F}{F_{y1}}}-1\right)\right]} \tag{1.45}$$

$$c' = \frac{1}{1+2\cdot\frac{r_0^2}{L_s}\cdot\int_0^{x_l}\frac{dx}{\left(R+r_0-\sqrt{R^2-x^2}\right)^2}} \tag{1.46}$$

For the specimen dimensions shown in Fig. 1.6, $r_0 = 1.59$ mm, $x_l = R = 3.18$ mm, and $L_s = 6.35$ mm, the specimen strain correction factor, c', for ***Region I***, is a constant, $c' = 0.62$.

Eq. (1.46) can also be rewritten as

$$c' = \frac{1}{1+2\cdot\frac{R}{L_s}\cdot\int_0^{\frac{x_l}{R}}\frac{d\frac{x}{R}}{\left(\frac{R}{r_0}+1-\frac{R}{r_0}\cdot\sqrt{1-\left(\frac{x}{R}\right)^2}\right)^2}} \tag{1.47}$$

which suggests that the correction factor, c', depends on the tensile specimen dimensions, $\frac{R}{r_0}$, $\frac{x_l}{R}$, and $\frac{R}{L_s}$. If the same specimen aspect ratio, $\frac{L_s}{2r_0} = 2$, is maintained, the correction factor, c', depends on $\frac{R}{r_0}$ and $\frac{x_l}{R}$, as shown in Fig. 1.16. With increasing the value of $\frac{R}{r_0}$, equivalent to decreasing the value $\frac{R}{L_s}$ with the same aspect ratio, or decreasing the value of $\frac{x_l}{R}$, the value of the correction factor, c' increases, which means decreased error in the specimen strain (or modulus of elasticity) without correction. The curves shown in Fig. 1.16 can also be used to optimize tensile specimen design for Kolsky tension bar tests.

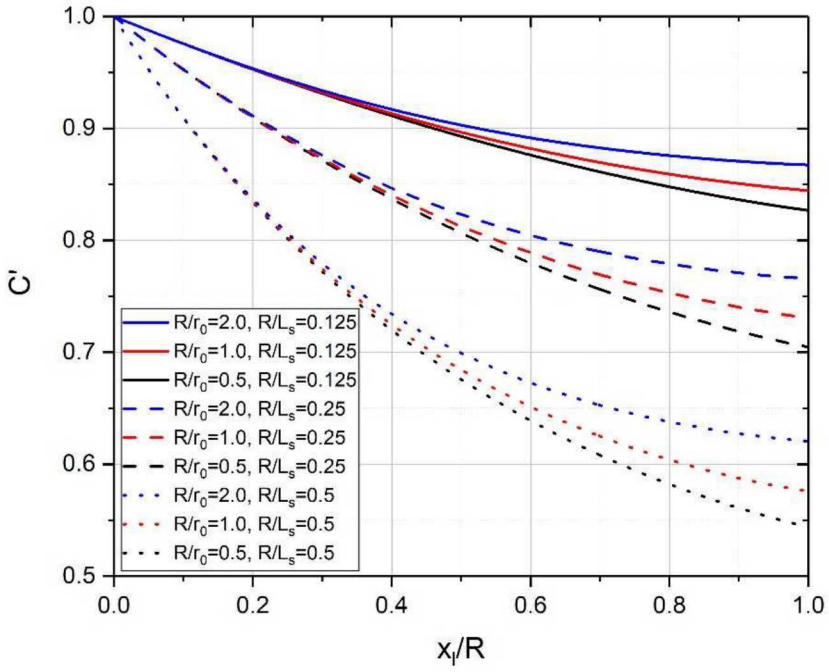

Figure 1.16. Effect of cylindrical tensile specimen design on the correction factor, c' [111].

The corrected specimen strains maintain continuity at $\sigma = \sigma_{y1}$ (or $F = F_{y1}$), where specimen gage-section deformation transits from ***Region I*** to ***Region II*** (at yield), or from ***Region II*** to ***Region III***. In addition, the corrected specimen strain also maintains continuity at the onset of necking, $F = F_{ult}$, where the specimen deformation transits from ***Region III*** to ***Region IV***.

For reference, the indefinite integral, $\int \frac{dx}{\left(R + r_0 - \sqrt{R^2 - x^2}\right)^2}$, evaluates to

$$\int \frac{dx}{\left(R + r_0 - \sqrt{R^2 - x^2}\right)^2} =$$

$$\left(\frac{\sqrt{r_0}\, x (r_0 + R)\left(r_0 + R + \sqrt{r_0^{\,2} + R^2}\right)}{R^2 (r_0 + 2R)\left(r_0^{\,2} + x^2 + 2 r_0 R\right)} + \frac{\tan^{-1}\left(\dfrac{x(r_0 + R)}{\sqrt{r_0}\sqrt{r_0 + 2R}\sqrt{R^2 - x^2}} \right)}{(r_0 + 2R)^{3/2}} + \frac{\tan^{-1}\left(\dfrac{x}{\sqrt{r_0}\sqrt{r_0 + 2R}} \right)}{(r_0 + 2R)^{3/2}} \right) R^2 r_0^{\,-3/2}$$

(1.48)

For a material without significant upper or lower yield, $F_{y1} = F_{y2} = F_y$, Eq. (1.44) becomes

$$\varepsilon = \begin{cases} c' \cdot \dfrac{\Delta L}{L_s} & \text{(Region I)} \\ \dfrac{F_y}{E_s \cdot \pi \cdot r_0^2} + \dfrac{\Delta L - \dfrac{2 \cdot F}{E_s \cdot \pi} \cdot \int_{x_0}^{x_l} \dfrac{dx}{\left(R + r_0 - \sqrt{R^2 - x^2}\right)^2} - \dfrac{F_y}{E_s \cdot \pi \cdot r_0^2} \cdot \left(2x_0 + L_s\right)}{\dfrac{2 \cdot F \cdot r_0^2 \cdot \int_0^{x_0} \dfrac{dx}{\left(R + r_0 - \sqrt{R^2 - x^2}\right)^2} - 2 \cdot F_y \cdot x_0}{F - F_y} + L_s} & \text{(Region III)} \\ \varepsilon\big|_{F=F_{ult}} + \dfrac{\Delta L - \Delta L\big|_{F=F_{ult}}}{L_s} + \dfrac{F_{ult} - F}{E_s \cdot \pi \cdot r_0^2} \cdot \left(\dfrac{1}{c'} - 1\right) & \text{(Region IV)} \end{cases} \tag{1.49}$$

For a material possessing perfect plasticity, Eq. (1.44) or (1.49) can be further simplified as

$$\varepsilon = \begin{cases} c' \cdot \dfrac{\Delta L}{L_s} & \text{(Region I)} \\ \dfrac{\Delta L}{L_s} - \dfrac{F_y}{E_s \pi r_0^2}\left(\dfrac{1}{c'} - 1\right) & \text{(Region III)} \\ \varepsilon_{necking} + \dfrac{\Delta L - \Delta L_{necking}}{L_s} + \dfrac{F_y - F}{E_s \cdot \pi \cdot r_0^2} \cdot \left(\dfrac{1}{c'} - 1\right) & \text{(Region IV)} \end{cases} \tag{1.50}$$

where $\varepsilon_{necking}$ and $\Delta L_{necking}$ are corrected specimen strain and measured total displacement at onset of necking. Considering

$$\frac{F_y}{E_s \pi r_0^2} = \varepsilon_y = c' \frac{\Delta L_{yield}}{L_s} \tag{1.51}$$

where $\Delta L_{necking}$ is measured total displacement at yield. Eq. (1.44) is rewritten as

$$\varepsilon = \begin{cases} c' \cdot \dfrac{\Delta L}{L_s} & \text{(Region I)} \\ \dfrac{\Delta L - (1-c') \cdot \Delta L_{yield}}{L_s} & \text{(Region III)} \\ \varepsilon_{necking} + \dfrac{\Delta L - \Delta L_{necking}}{L_s} + \dfrac{F_y - F}{E_s \cdot \pi \cdot r_0^2} \cdot \left(\dfrac{1}{c'} - 1 \right) & \text{(Region IV)} \end{cases} \quad (1.52)$$

Differentiation of the corrected specimen strain yields the strain rate over the specimen gage section.

The numerical correction presented earlier only applies to cylindrical specimens. However, following the same procedure, a numerical correction for sheet specimens could be obtained. Due to the complexity of sheet specimen mounting methods, numerically corrected specimen strain may not be accurate because in addition to the non-gage section, the material at the specimen ends deform depending on the mounting method. Although finite element analysis is an approach to correct specimen strain over the gage section [100], direct displacement or strain measurement over the gage section is highly recommended.

Pulse Shaping in a Kolsky Tension Bar Test

The procedure of conducting a Kolsky tension bar experiments is similar to Kolsky compression bar experiments extensively presented in the book by Chen and Song [18]. Appropriate pulse shaping is vital to ensure dynamic stress equilibrium and constant strain rate. While a short gage length helps the sample equilibrate quickly, a rise time on the order of 100 μs or longer is needed for the specimen to reach dynamic stress equilibrium. Constant strain rate deformation, as illustrated in Fig. 1.17, is achieved by altering the profile of the incident pulse. If a Kolsky tension bar shown in Fig. 1.1(c) is used, one can follow the same pulse shaping design for Kolsky compression bar tests [18]. In general, a nearly square pulse results in constant strain rate for materials possessing near perfectly plastic response (Fig. 1.2) [79-83]. However, when the material possesses significant work hardening behavior, a bilinear incident pulse is necessary to achieve constant strain rate (Fig. 1.2) [84].

The complexities of the specimen deformation in Kolsky tension bar experiments limits rapid determination of the specimen strain rate during experimentation. Unlike Kolsky compression bar experiments where the reflected pulse can be used to quickly check the specimen strain rate, neither the conventional strain gage method nor differentiation of the laser extensometer displacement measurement represents the strain rate history in a tension experiment [111]. This results in a more complex pulse shaping design as well as expansion of the iterative process of pulse shaping to achieve constant strain rate deformation.

Interpretation of Dynamic Tensile Response of Metallic Materials

Understanding the dynamic tensile stress-strain curves experimentally obtained from a Kolsky tension bar is straightforward, but special attention needs to be paid to strain rate effects on quantities such as yield and ultimate strength. As in a typical Kolsky compression bar test, time is required for the strain rate to ramp from zero to the desired constant value [112]. During the strain rate ramp, the actual strain rate is lower than the constant or nominal value typically reported for the entire experiment. The material commonly yields during the strain rate ramp before a constant value is reached. Therefore, the actual strain rate at yield must be used to determine strain rate effects, even

though the strain rate has not yet reached a constant value [113]. Otherwise, the strain rate effect would be misinterpreted. Similarly, the actual strain rates used determine other quantities such as flow stress at different strain values as well as ultimate strength are recommended to determine strain rate effects, as shown in Fig. 1.17. As shown in Fig. 1.17, before necking occurred at 20.5% true plastic strain, the engineering strain rate was slightly lower than 1500 s^{-1} and did not maintain at a perfect constant value. Notably, the strain rate at yield was only ~200 s^{-1}, which is significantly lower than the nominal value of 1500 s^{-1}. Using a nominal constant value of strain rate would thus generate significant uncertainties.

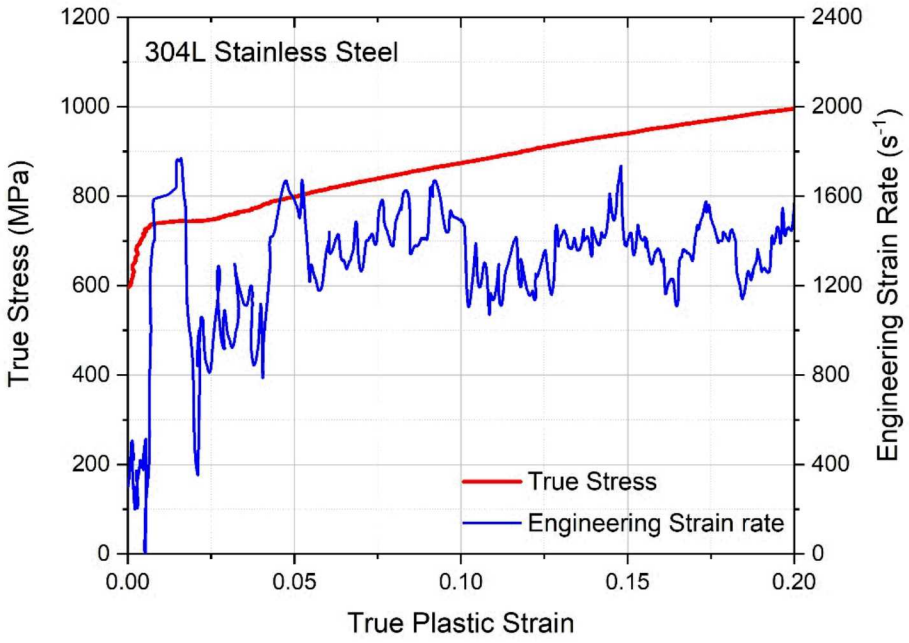

Figure 1.17. Actual stress and strain rate histories in the specimen [113]

When necking occurs, the specimen deformation becomes highly localized. The localization of specimen strain also results in localized strain rate, which can be significantly higher than the nominal rate. Therefore, true strain and strain rate are more representative of the actual specimen deformation and deformation rate over the necking region. High-speed DIC can provide the full-field deformation over the entire gage section, making it possible to directly extract the localized strain and strain rate. In addition to DIC, the true strain of the tensile specimen during necking can be calculated with instantaneous cross-sectional area of the specimen (Eq. (1.47)) with high-speed imaging of the neck profile or the LORD method presented earlier. The true strain rate is thus

$$\dot{\varepsilon}_{true} = -\frac{\dot{A}}{A} \tag{1.53}$$

The true strain rate over the necking region could be 5 to 9 times or even one order higher in magnitude than the nominal strain rate [113-115]. This highly magnified strain rate over the necking region needs to be considered during the calibration process of strain-rate-dependent material models.

Stress triaxiality is also generated within the neck. Therefore, the nominal post-necking stress-strain response is highly dependent on specimen geometry, especially gage length. For the same material, tensile specimens with different gage lengths possess different nominal post necking stress-strain response [116]. Although the nominal post-necking stress-strain response can be used for material model calibration, true stress-strain response is preferred to describe the actual material response. Due to stress triaxiality over the necking region, Eq. (1.43) needs to be corrected to calculate the equivalent stress in the specimen.

$$\sigma_{eq} = k \cdot \sigma_{true} \tag{1.54}$$

where k is a correction factor for triaxiality. The Bridgman correction is used for cylindrical specimens to determine the triaxiality factor, k, based on the assumptions of uniform strain distribution in the minimum section and a longitudinal grid line deformed into a curve at the neck (Fig. 1.18) [107, 117, 118],

$$k = \frac{1}{\left(1+\frac{2R}{a}\right)\cdot \ln\left(1+\frac{a}{2R}\right)} \tag{1.55}$$

where a and R are the radii at the minimum cross section and necking, as illustrated in Fig. 1.18, Eq. (1.55) requires instantaneous measurement of the minimum diameter and curvature of the tensile specimen during necking, which are usually obtained from high-speed imaging. There has been a debate about the accuracy of the Bridgman correction due to the underlying assumptions. [114, 119] A polynomial named $MLR_{\sigma}\left(\varepsilon_{true}-\varepsilon_{N}\right)$ was developed by Mirone [114, 119] to estimate the equivalent stress averaged over the neck cross-section from the experimentally measured true-stress, σ_{true},

$$\sigma_{eq} = \sigma_{True} \cdot MLR_{\sigma}\left(\varepsilon_{True}-\varepsilon_{N}\right) \tag{1.56}$$

where ε_N is the onset strain of necking, and

$$MLR_{\sigma}\left(\varepsilon_{True}-\varepsilon_{N}\right) = 1-0.6058\cdot\left(\varepsilon_{True}-\varepsilon_{N}\right)^{2}+0.6317\cdot\left(\varepsilon_{True}-\varepsilon_{N}\right)^{3}-0.2107\cdot\left(\varepsilon_{True}-\varepsilon_{N}\right)^{4} \tag{1.57}$$

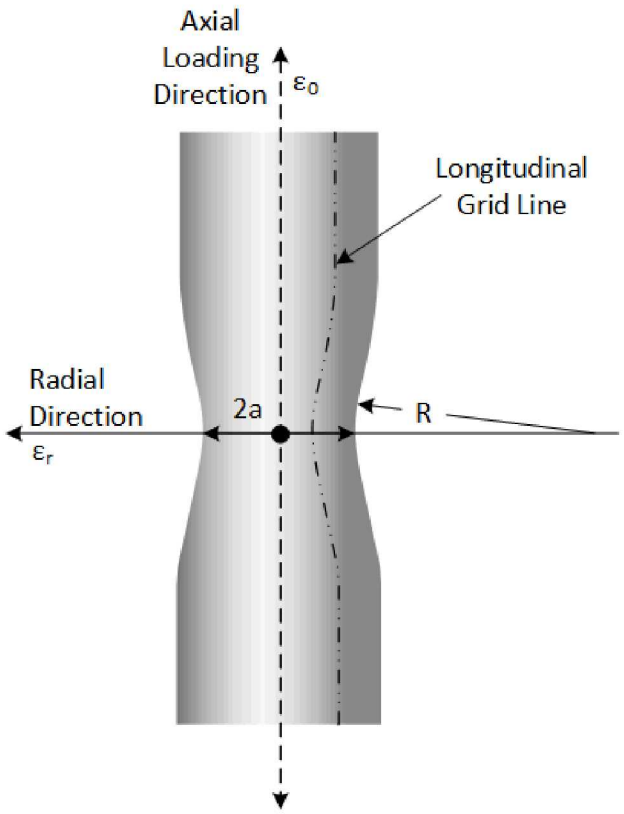

Figure 1.18. Bridgman correction for necking.

The triaxiality correction for sheet tensile specimens is more complicated due to higher strain gradients than those observed in axisymmetric specimens [120]. A modeling and numerical simulation approach is usually needed to determine the ductility and true stress triaxiality in sheet tensile specimens.

Interrupted Kolsky Tension Bar Experiments

Just as in Kolsky compression bar tests, the specimen in a Kolsky tension bar test may be subjected to multiple loadings until failure occurs. For investigations of material behavior such as rate dependent behavior on microstructure or damage evolution, subjecting the specimen to a controlled strain level prior to fracture may be desirable. Nemat-Nesser et al. [53] developed a momentum trapped Kolsky tension bar for such interrupted tensile loading shown schematically in Fig. 1.19. Although this design was originally developed for a tubular striker tension bar (Fig. 1.1(b)), the concept is applicable to the solid striker method shown in Fig. 1.1(c). In this method, a mechanical-impedance-matched momentum bar is placed next to the transfer flange for the method in Fig. 1.1(b) or the end cap for the method in Fig. 1.1(c), with a precise gap in between. While a tensile pulse is generated, the incident bar moves toward the momentum trap bar. The gap is closed before the reflected pulse propagates back to the interface allowing the reflected pulse to transmit into the momentum trap bar rather than being reflected back into the incident bar to subject the tensile specimen to a secondary tensile loading.

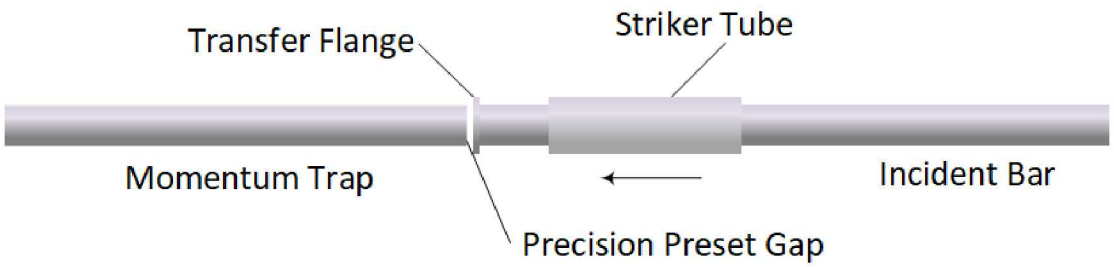

Figure 1.19. Dynamic tensile recovery experiment design

Another option for interrupted dynamic tensile tests is to use conventional Kolsky tension bars with a specially designed fixture and/or specimen to restrict the deformation subjected to the tensile specimen. Fig. 1.20(a) shows the design of different fixtures for interrupted dynamic tensile tests. The fixture includes an external cylindrical tube with screws to adjust the total allowable displacement to the specimen while stepped ends of the incident and transmission bars act as stoppers, and damping rings absorb excessive impact energy [52]. Instead of using the damping rings, a notched or straight section (Fig. 1.20(b)) with a larger diameter than the gage section was added to the specimen as sacrificial pieces to absorb the excessive impact energy [60, 121].

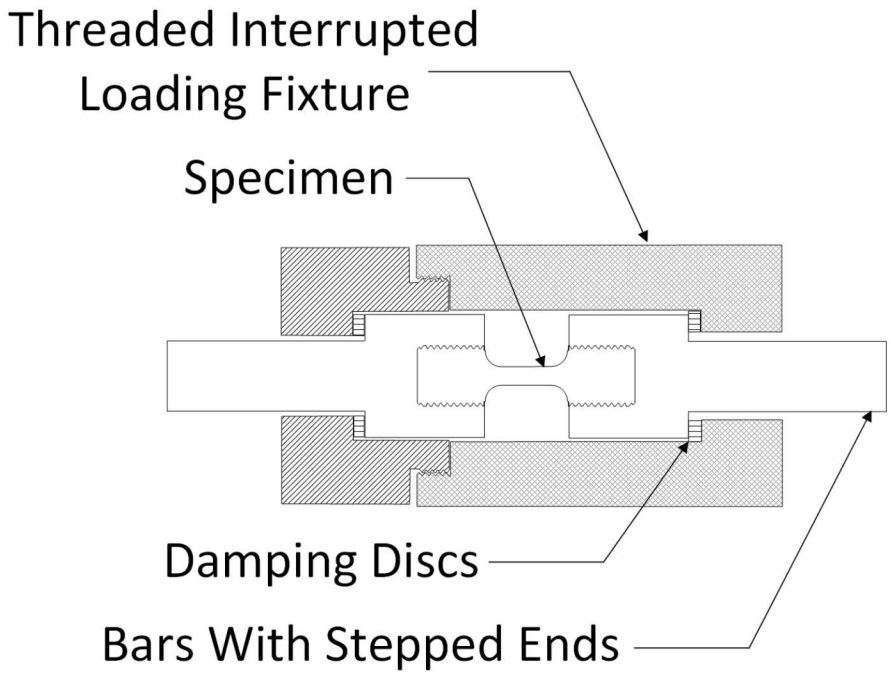

(a)

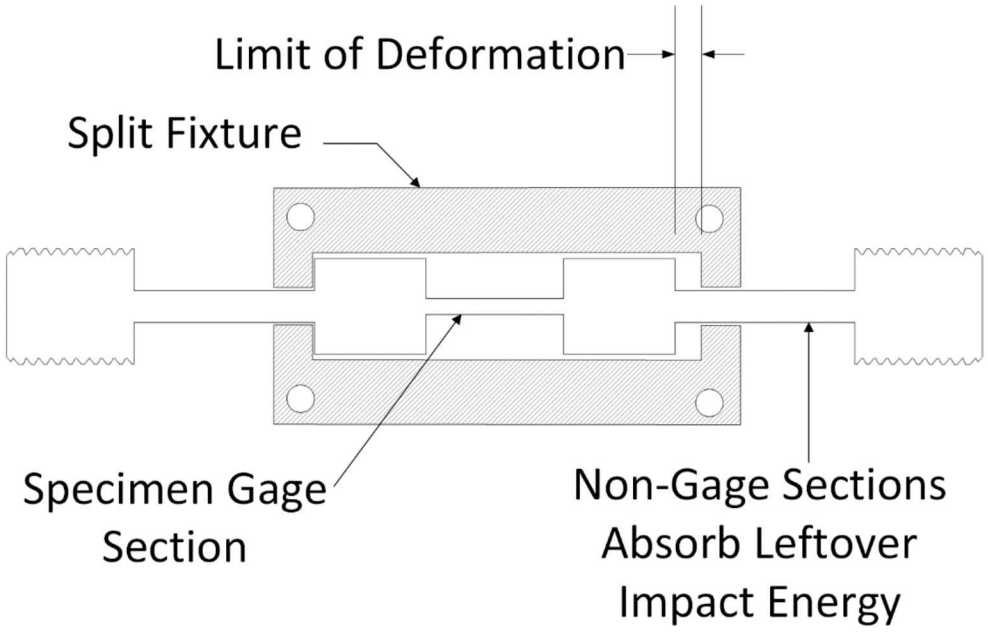

(b)

Figure 1.21. Fixture and specimen design for dynamic interrupted tensile experiments

Summary

Kolsky tension bar experiments on metallic materials are more complicated and challenging than Kolsky compression bar experiments with regard to bar and specimen design, experimental execution, and measurement to data interpretation. The Kolsky tension bar itself must be carefully designed to generate reliable tensile pulses. The tensile specimen must be designed to achieve stress equilibrium while maintaining a uniaxial stress state in the tensile specimen. Attention needs to be paid to the specimen strain measurement. Appropriate interpretation of the dynamic tensile material response is essential to determine strain-rate effect, as well as necking response to develop reliable strain-rate-dependent material models, calibration, and validation. Interrupted Kolsky tension bar experiments are also useful for investigation of strain-rate-dependent damage evolution, structure-property relationship, as well as multiscale failure and fracture.

Acknowledgement

The authors thank Ms. Sabrina Fleming and Ms. Laura Sowko for their assistance on the preparation for the manuscript.

Sandia National Laboratories is a multimission laboratory managed and operated by National Technology and Engineering Solutions of Sandia, LLC, a wholly owned subsidiary of Honeywell International, Inc., for the U.S. Department of Energy's National Nuclear Security Administration under contract DE-NA0003525. The views expressed in the article do not necessarily represent the views of the U.S. Department of Energy or the United States Government.

References

[1] Altynova, M., Hu, X., and Daehn, G. S., 1996, "Increased ductility in high velocity electromagnetic ring expansion," **Metallurgical and Materials Transactions A**, 27A:1837-1844.

[2] Kahana, E., Ben-Artzy, A., Sadot, O., and Shneck, R. Z., 2015, "Microstructural evolution of AZ31 magnesium alloy after high strain rate expanding rings tests," **Materials Science & Engineering A**, 641:274-280.

[3] Ma, H., Huang, L., Wu, M., and Li, J., 2014, "Dynamic ductility and fragmentation for aluminum alloy using electromagnetic ring expansion," **Procedia Engineering**, 81:787-792.

[4] Samuha, S., Kahana, E., Sadot, O., and Shneck, R. Z., 2018, "Improved formability of Mg-AZ80 alloy under s high strain rate in expanding-ring experiments," **Materials**, 11:329.

[5] Campbell, G. H., Archbold, G. C., Hurricane, O. A., and Miller, P.L., 2007, "Fragmentation in biaxial tension," **Journal of Applied Physics**, 101:033540.

[6] Dekel, E., Eliezer, S., Henis, Z., Moshe, E., Ludmirsky, A., and Goldberg, I. B., 1998, "Spallation model for the high strain rates range," **Journal of Applied Physics**, 84:4851.

[7] Escobedo, J. P., and Gupta, Y. M., 2010, "Dynamic tensile response of Zr-based bulk amorphous alloys: fracture morphologies and mechanisms," **Journal of Applied Physics**, 107:123502.

[8] Turneaure, S. J., Dwivedi, S. K., and Gupta, Y. M., 2007, "Shock-wave induced tension and spall in a zirconium-based bulk amorphous alloy," **Journal of Applied Physics**, 101:043514.

[9] Bonora, N., Bourne, N., Ruggiero A., Iannitti, G., and Testa, G., 2017, "Investigation on grain size effect in high strain rate ductility of 1100 pure aluminum," **AIP Conference Proceedings**, 1793:110003.

[10] Cao, F., Cerreta, E. K., Trujillo, C. P., and Gray, G. T., III, 2008, "Dynamic tensile extrusion response of tantalum," **Acta Materialia**, 56:5804-5817.

[11] Gray, G .T., Cerreta, E., Yablinsky, C. A., Addessio, L. B., Henrie, B. L., Sencer, B. H., Burkett, M., Maudlin, P. J., Maloy, S. A., Trujillo, C. P., and Lopez, M. F., 2006, "Influence of shock prestraining and grain size on the dynamic-tensile-extrusion response of copper: experiments and simulation," **AIP Conference Proceedings**, 845:725.

[12] Hörnqvist, M., Mortazavi, N., Halvarsson, M., Ruggiero, A., Iannitti, G., and Bonora, N., 2015, "Deformation and texture evolution of OFHC copper during dynamic tensile extrusion," **Acta Materialia**, 89:163-180.

[13] Park, K-T., Park, L., Kim, H. J., Kim, S. B., and Lee, C. S., 2013, "Dynamic tensile extrusion behavior of coarse grained and ultrafine grained OFHC Cu," **Materials Science & Engineering A**, 569:61-70.

[14] Kolsky, H., 1949, "An investigation of the mechanical properties of materials at very high rates of loading," **Proceedings of the Royal Society of London**, B62:676-700.

[15] Harding, J., Wood, E. O., Campbell, J. D., 1960, "Tensile testing of materials at impact rates of strain," **Journal of Mechanical Engineering and Sciences**, 2:88-96.

[16] Al-Mousawi, M. M., Reid, S. R., and Deans, W. F., 1997, "The use of the split Hopkinson pressure bar techniques in high strain rate materials testing," **Proceedings of the Institution of Mechanical Engineers,** Part C, 211:273-292.

[17] Othman, R. (ed.), 2018, *The Kolsky-Hopkinson bar machine*, Springer.

[18] Chen, W., and Song, B., 2011, *Split Hopkinson (Kolsky) Bar: Design, Testing and Applications*, Springer.

[19] Hauser, F. E., 1966, "Techniques for measuring stress-strain relations at high strain rates," **Experimental Mechanics**, 6:395-402.

[20] Harding, J., and Welsh, L. M., 1983, "A tensile testing technique for fiber-reinforced composites at impact rates of strain," **Journal of Material Science**, 18:1810-1826.

[21] Roth, C. C., and Mohr, D., 2014, "Effect of strain rate on ductile fracture initiation in advanced high strength steel sheets: experiments and modeling," **International Journal of Plasticity**, 56:19-44.

[22] Roth, C. C., Gary, G., and Mohr, D., 2015, "Compact SHPB system for intermediate and high strain rate plasticity and fracture testing of sheet metal," **Experimental Mechanics**, 55:1803-1811.

[23] Dunand, M., Gary, G., and Mohr, D., 2013, "Load-inversion device for the high strain rate tensile testing of sheet materials with Hopkinson pressure bars," **Experimental Mechanics**, 53:1177-1188.

[24] Lindholm, U. S., and Yeakley, L. M., 1968, "High strain rate testing: tension and compression," **Experimental Mechanics**, 11:181-191.

[25] Nicholas, T., 1981, "Tensile testing of materials at high rates of strain," **Experimental Mechanics**, 21:177-188.

[26] Bobbili, R., Madhu, V., and Gogia, A. K., 2016, "Tensile behaviour of aluminum 7017 alloy at various temperatures and strain rates," **Journal of Materials Research and Technology**, 5:190-197.

[27] Panowicz, R., and Janiszewski, J., 2016, "Tensile split Hopkinson bar technique: numerical analysis of the problem of wave disturbance and specimen geometry selection," **Metrology and Measurement Systems**, 23:425-436.

[28] Mao, P., Liu, Z., and Wang, C., 2012, "Texture effect on high strain rates tension and compression deformation behavior of extruded AM30 alloy," **Materials Science and Engineering A**, 539:13-21.

[29] Mott, P. H., Twigg, J. N., Roland, D. F., Schrader, H. S., Pathak, J. A., and Roland, C. M., 2007, "High-speed tensile test instrument," **Review of Scientific Instruments**, 78:045105.

[30] Sturges, J. L., and Cole, B. N., 2001, "The flying wedge: a method for high-strain-rate tensile testing. Part 1. Reasons for its development and general description," **International Journal of Impact Engineering**, 25:251-264.

[31] Mir, A. A., Barton, D. C., Andrews, T. D., and Church, P., 2005, "Anisotropic ductile failure in free machining steel at quasi-static and high strain rates," **International Journal of Fracture**, 133:289-302.

[32] Kawata, K., Hashimoto, S., Kurokawa, K., Kanayama, N., 1979, "A new testing method for the characterization of materials in high-velocity tension," In: J. Harding (ed.), Mechanical Properties at High Rates of Strain, **Institute of Physics Conference Series**, 47:71-80.

[33] Li, M., Wang, R., and Han, M.B., 1993, "A Kolsky bar: tension, tension-tension," **Experimental Mechanics**, 33:7-14.

[34] Chen, X., Wang, Y., Gong, M., and Xia, Y., 2004, "Dynamic behavior of SUS304 stainless steel at elevated temperatures," **Journal of Materials Science**, 39:4869-4875.

[35] Zhang, J., Wang, Y., Zan, X., and Wang, Y., 2015, "The constitutive responses of Ti-6.6Al-3.3Mo-1.8Zr-0.29Si alloy at high strain rates and elevated temperatures," **Journal of Alloys and Compounds**, 647:97-104.

[36] Zhang, B., Wang, J., Wang, Y., Li, Z., and Wang, Y., 2019, "Dynamic strain-rate effect on uniaxial tension deformation of Ti5Al2.5Sn α-titanium alloy at various temperatures," **Materials at High Temperatures**, 36:479-488.

[37] Zhang, B, Wang, J., Wang, Y., Wang, Y., and Li, Z., 2019, "Strain-rate-dependent tensile response of Ti-5Al-2.5Sn Alloy," **Materials**, 12:659.

[38] Nie, H., Suo, T., Shi, X., Liu, H., Li, Y., and Zhao, H., 2018, "Symmetric split Hopkinson compression and tension tests using synchronized electromagnetic stress pulse generators," **International Journal of Impact Engineering**, 122:73-82.

[39] Staab, G. H., and Gilat, A., 1991, "A direction-tension split Hopkinson bar for high-strain-rate testing," **Experimental Mechanics**, 31:232-235.

[40] Albertini, C., Cadoni, E., and Solomos, G., 2014, "Advances in the Hopkinson bar testing of irradiated/non-irradiated nuclear materials and large specimens," **Philosophical Transactions of The Royal Society A**, 372:20130197.

[41] Solomos, G., Albertini, C., Labibes, K., Pizzinato, V., and Viaccoz, B., 2004, "Strain rate effects in nuclear steels at room and higher temperatures," **Nuclear Engineering and Design**, 229:139-149.

[42] Cadoni, E., Dotta, M., Forni, D., and Spätig, P., 2011, "Strain-rate behavior in tension of the tempered martensitic reduced activation steel Eurofer97," **Journal of Nuclear Materials**, 414:360-366.

[43] Cadoni, E., Fenu, L, and Forni, D., 2012, "Strain rate behaviour in tension of austenitic stainless steel used for reinforcing bars," **Construction and Building Materials**, 35:399-407.

[44] Cadoni, E., Dotta, M., Forni, D., and Tesio, N., 2015, "High strain rate behaviour in tension of steel B500A reinforcing bar," **Materials and Structures**, 48:1803-1813.

[45] Chen, Y., Clausen, A.H., Hopperstad, O.S., and Langseth, M., 2011, "Application of a split-Hopkinson tension bar in a mutual assessment of experimental tests and numerical predictions," **International Journal of Impact Engineering**, 38:824-836.

[46] Forni, D., Chiaia, B., and Cadoni, E., 2016, "Strain rate behaviour in tension of S355 steel: base for progressive collapse analysis," **Engineering Structures**, 119:164-173.

[47] Haugou, G., Leconte, N., and Morvan, H., 2016, "Design of a pre-stretched tension Hopkinson bar device: configuration, tail corrections, and numerical validation," **International Journal of Impact Engineering**, 97:89-101.

[48] Li, Y., Ramesh, K.T., and Chin, E.S.C., 2004, "Comparison of the plastic deformation and failure of A359/SiC and 6061-T6/Al_2O_3 metal matrix composites under dynamic tension," **Materials Science and Engineering A**, 371:359-370.

[49] Li, Y., Ramesh, K. T., and Chin, E. S. C., 2007, "Plastic deformation and failure in A359 aluminum and an A359-SiC_p MMC under quasistatic and high-strain-rate tension," **Journal of Composite Materials**, 41:27-40.

[50] Tarigopula, V., Hopperstad, O. S., Langseth, M., Clausen, A. H., and Hild, F., 2008, "A study of localisation in dual-phase high-strength steels under dynamic loading using digital image correlation and FE analysis," **International Journal of Solids and Structures**, 45:601-619.

[51] Vilamosa, V., Clausen, A. H., Fagerholt, E., Hopperstad, O. S., and Børvik, T., 2014, "Local measurement of stress-strain behaviour of ductile materials at elevated temperatures in a split-Hopkinson tension bar system," **Strain**, 50:223-235.

[52] González-Lezcano, R. A., and del Río, J. M., 2015, "Numerical analysis of the influence of the damping rings' dimensions on interrupted dynamic tension experiment results," **Journal of Strain Analysis**, 50:594-613.

[53] Nemat-Nasser, S., Isaacs, J. B., and Starrett, J. E., 1991, "Hopkinson techniques for dynamic recovery experiments," **Proceedings of Royal Society of London A**, 435:371-391.

[54] Hueto, F., Hokka, M., Sancho, R., Rämö, J., Östman, K., Gálvez, F., and Kuokkala, V.-T., 2017, "High temperature dynamic tension behavior of titanium tested with two different methods," **Procedia Engineering**, 197:130-139.

[55] Huh, H., Kang, W. J., and Han, S. S., 2002, "A tension split Hopkinson bar for investigating the dynamic behavior of sheet metals," **Experimental Mechanics**, 42:8-17.

[56] Jing, L., Han, L., Zhao, L, and Zhang, Y., 2016, "The dynamic tensile behavior of railway wheel steel at high strain rates," **Journal of Materials Engineering and Performance**, 25:4959-4966.

[57] Ledford, N., Paul, H., Ganzenmüller, G., May, M., Höfemann, M., Otto, M., and Petrinic, N., 2015, "Investigations on specimen design and mounting for split Hopkinson tension bar (SHTB) experiments," **EPJ Web of Conference**, 94:01049.

[58] Li, L.-Y., and Molyneaux, T.C.K., 1995, "Dynamic constitutive equations and behaviour of brass at high strain rates," **Proceedings of the Institution of Mechanical Engineers, Part C: Journal of Mechanical Engineering Science**, 209:287-293.

[59] Li, P.-H., Guo, W.-G., Yuang, K.-B., Su, Y., Wang, J.-J., Lin, X., and Li, Y.-P., 2018, "Effects of processing defects on the dynamic tensile mechanical behavior of laser-solid-formed Ti-6Al-4V," **Materials Characterization**, 140:15-29.

[60] Ma, D., Chen, D., Wu, S., Wang, H., You, Y., and Cai, C., 2010, "An interrupted tensile testing at high strain rates for pure copper bars," **Journal of Applied Physics**, 108:114902.

[61] Ma. D., Chen, D., Wu, S., Wang, H., You, Y., Cai, C., and Deng, T., 2012, "Analysis of thermoviscoplastic effects on dynamic necking of pure copper bars during impact tension," **International Journal of Nonlinear Sciences and Numerical Simulation**, 13:125-136.

[62] Miao, Y., Du, B., Ma, C., Hu, H., and Deng, Q., 2019, "Some fundamental problems concerning the measurement accuracy of the Hopkinson tension bar technique," **Measurement Science and Technology**, 30:055009.

[63] Prabowo, D. A., Kariem, M. A., and Gunawan, L., 2016, "The effect of specimen dimension on the results of the split-Hopkinson tension bar testing," **Procedia Engineering**, 173:608-614.

[64] Shamchi, S. P., Queirós de Melo, F. J. M., Tavares, P. J., and Moreira, P. M .G. P., 2019, "Thermomechanical characterization of Alclad AA2024-T3 aluminum alloy using split Hopkinson tension bar," **Mechanics of Materials**, 139:103198.

[65] Shazly, M., Prakash, V., and Draper, S., 2004, "Mechanical behavior of Gamma-Met PX under uniaxial loading at elevated temperatures and high strain rates," **International Journal of Solids and Structures**, 41:6485-6503.

[66] Shin, H., Lee, J.-H., Kim, J.-B., and Sohn, S.-I., 2020, "Design guidelines for the striker and transfer flange of a split Hopkinson tension bar and the origin of spurious waves," **Proceedings of the Institution of Mechanical Engineers, Part C: Journal of Mechanical Engineering Science**, 234:137-151.

[67] Su, J., Guo, W., Meng, W., and Wang, J., 2013, "Plastic behavior and constitutive relations of DH-36 steel over a wide spectrum of strain rates and temperatures under tension," **Mechanics of Materials**, 65:76-87.

[68] Takahashi, Y., Daimaruya, M., Kobayashi, H., Tsuda, H., and Fujiki, H., 2008, "Impact tensile properties of YAG laser welded butt joints made by different steel sheets for vehicles," **International Journal of Modern Physics B**, 22:1712-1717.

[69] Thakur, A., Nemat-Nasser, S., and Vecchio, K.S., 1996, "Dynamic Bauschinger effect," **Acta Materialia**, 44:2797-2807.

[70] Wang, H., Zhang, W., Ma, D., Ma, B., Chen, D., Yang, X., and Fan, C., 2017, "Dynamic response of a Q&P steel to high-strain-rate tension," **Acta Mechanica Solida Sinica**, 30:484-492.

[71] Wu, S. Y., Bie, B. X., Fan, D., Sun, T., Fezzaa, K., Feng, Z. D., Huang, J. Y., and Luo, S. N., 2018, "Dynamic shear localization of a titanium alloy under high-rate tension characterized by X-ray digital image correlation," **Materials Characterization**, 137:58-66.

[72] Xue, Q., Benson, D., Meyers, M.A., Nesterenko, V.F., and Olevsky, E.A., 2003, "Constitutive response of welded HSLA 100 steel," **Materials Science and Engineering**, A354:166-179.

[73] Yokoyama, T., 2003, "Experimental determination of impact tensile properties of adhesive butt joints with the split Hopkinson bar," **Journal of Strain Analysis**, 38:233-245.

[74] Yu, H., Guo, Y., Zhang, K., and Lai, X., 2009, "Constitutive model on the description of plastic behavior of DP600 steel at strain rate from 10^{-4} to 10^{3} s^{-1}," **Computational Materials Science**, 46:36-41.

[75] Zhang, L, Gour, G., Petrinic, N., and Pellegrino, A., 2020, "Rate dependent behaviour and dynamic strain localisation of three novel impact resilient titanium alloys: experiments and modelling," **Materials Science & Engineering A**, 771:138552.

[76] Zhou, B., Pan, Y., Shi, Q., and Fu, X., 2019, "Effect of high strain rates and different orientations on tensile behavior and microcosmic evolution of Ti-6Al-4V sheet," **Materials Research Express**, 6:098001.

[77] Guzman, O., Frew, D. J., and Chen, W., 2011, "A Kolsky tension bar technique using a hollow incident tube," **Measurement Science and Technology**, 22:045703.

[78] Song, B., Antoun, B. R., Connelly, K., Korellis, J., and Lu, W.-Y., 2011, "Improved Kolsky Tension Bar for High-rate Tensile Characterization of Materials," **Measurement Science and Technology**, 22:045704.

[79] Song, B., Antoun, B. R., and Jin, H., 2013, "Dynamic Tensile Characterization of a 4330-V Steel," **Experimental Mechanics**, 53:1519-1529.

[80] Song, B., Wakeland, P. E., Furnish, M., 2015, "Dynamic Tensile Characterization of Vascomax Maraging C250 and C300 Alloys", **Journal of Dynamic Behavior of Materials**, 1:153-161.

[81] Song, B., Nelson, K., Lipinski, R., Bignell, J., Ulrich, G. B., and George, E. P., 2015, "Dynamic High-Temperature Tensile Characterization of an Iridium Alloy with Kolsky Tension Bar Techniques," **Journal of Dynamic Behavior of Materials**, 1:290-298.

[82] Sanborn, B., Song, B., Thompson, A., Reece, B., and Attaway, S., 2017, "High Strain Rate Tensile Response of A572 and 4140 Steel," **Procedia Engineering**, 197:33-41.

[83] Song, B., Nishida, E., Sanborn, B., Maguire, M., Adams, D. P., Carroll, J., Wise, J., Reedlunn, B., Bishop, J., and Palmer, T., 2017, "Compressive and Tensile Stress-Strain Responses of Additively Manufactured (AM) 304L Stainless Steel at High Strain Rates," **Journal of Dynamic Behavior of Materials**, 3:412-425.

[84] Song, B., Sanborn, B., Susan, D., Johnson, K., Dabling, J., Carroll, J., Brink, A., Grutzik, S., and Kustas, A., 2020, "Dynamic Tensile Response of a Fe-49Co-2V Alloy at Various Strain Rates and Temperatures," **Journal of Dynamic Behavior of Materials**, 6:224-235.

[85] Sun, X., Soulami, A., Choi, K. S., Guzman, O., and Chen, W., 2012, "Effects of sample geometry and loading rate on tensile ductility of TRIP800 steel," **Materials Science and Engineering A**, 541:1-7.

[86] Haugou, G., Leconte, N., and Morvan, H., 2015, "Separation of the elastic waves' system in pre-stretched bar devices," **EPJ Web of Conferences**, 94:01067.

[87] Chen, W., Lu, F., and Cheng, M., 2002, "Tension and compression tests of two polymers under quasi-static and dynamic loading," **Polymer Testing**, 21:113-121.

[88] Cheng, M., Chen, W., and Weerasooriya, T., 2009, "Mechanical behavior of bovine tendon with stress-softening and loading rate effects," **Advanced Theoretical and Applied Mechanics**, 2:59-74.

[89] Gerlach, R., Kettenbeil, C., and Petrinic, N., 2012, "A new split Hopkinson tensile bar design," **International Journal of Impact Engineering**, 50:63-67.

[90] Ganzenmüller, G.C., Blaum, E., Mohrmann, D., Langhof, T., Plappert, D., Ledford, N., Paul, H., and Hiermaier, S., 2017, "A simplified design for a split-Hopkinson tension bar with long pulse duration," **Procedia Engineering**, 197:109-118.

[91] Wang, L.-L., 2007, **Foundations of Stress Waves**. Elsevier

[92] ASTM (2009) Standard test methods for tension testing of metallic materials, ASTM standard E8/E8M-09.

[93] Godinger, A., Rotbaum, Y., Vaz-Romero, A., Rodríguez-Martínez, and Rittel, D., 2017, On the relation between shape imperfections of a specimen and necking growth rate under dynamic conditions, **International Journal of Engineering Sciences**, 119:278-287.

[94] Song, B., and Antoun, B., 2012, Pseudo stress response in Kolsky tension bar experiments, **Experimental Mechanics**, 52:525-528.

[95] Song, B., Sanborn, B., Susan, D., Johnson, K., Dabling, J., Carroll, J., Brink, A., Grutzik, S., and Kustas, A. B., 2020, Dynamic tensile response of a Fe-49Co-2V alloy at various strain rates and temperatures, **Journal of Dynamic Behavior of Materials** (online available)

[96] Qiu, Y., Loeffler, C. M., Nie, X., and Song, B., 2018, Improved Experimental and Diagnostic Techniques for Dynamic Tensile Stress-Strain Measurement with a Kolsky Tension Bar, **Measurement Science and Technology**, Vol. 29, 075201.

[97] Rusinek, A., and Klepaczko, J. R., 2003, Impact tension of sheet metals – effect of initial specimen length, **Journal de Physique IV France**, 110:329-334.

[98] Rusinek, A., Zaera, R., Klepaczko, J. R., and Cheriguene, R., 2005, Analysis of inertia and scale effects on dynamic neck formation during tension of sheet steel, **Acta Materialia**, 53:5387-5400.

[99] Rusinek, A., Cheriguene, R., Bäumer, Klepaczko, J. R., and Larour, P., 2008, Dynamic behaviour of high-strength sheet steel in dynamic tension: experimental and numerical analyses, **Journal of Strain Analysis for Engineering Design**, 43:37-53.

[100] Sanborn, B., Hudspeth, M., and Song, B., 2020, Dynamic tensile characterization of thin-sheet brittle metallic materials, **Experimental Techniques**, (accepted).

[101] Rhorer, R., 2016, Clamping-force application for Kolsky bar tension grips, In: **Dynamic Behavior of Materials, Volume 1** (B. Song, L. Lamberson, D. Casem, and J. Kimberley, eds.), Proceedings of the 2015 Annual Conference on Experimental and Applied Mechanics, Springer, pp.245-252.

[102] Kirk, C.D., Parab, N.D., Kedir, N., Guo, Z., Nie, Y., Paulson, S., Thomas, J., Fezzaa, K., Sun, T., and Chen, W., 2019, In-situ visualization of tensile failure in additively manufactured 316L stainless steel, **Experimental Mechanics**, 59:805-818.

[103] Nie, X., Song, B., and Loeffler, C. M., 2015, A Novel Splitting-Beam Laser Extensometer Technique for Kolsky Tension Bar Experiment, **Journal of Dynamic Behavior of Materials**, 1:70-74.

[104] Panowicz, R., Janiszewski, J., and Traczyk, M., 2017, Strain measuring accuracy with splitting-beam laser extensometer technique at split Hopkinson compression bar experiment, **Bulletin of the Polish Academy of Sciences**, 65:163-169.

[105] Seidt, J. D., Pereira, J. M., and Gilat, A., 2015, Influence of fabrication method on tensile response of split Hopkinson bar-sized specimens, **Journal of Testing and Evaluation**, 43:1563-1573.

[106] Huang, C., Chen, S., and Duan, Z., 2005, Real-time measurement on deformation fields of notched samples under impact tension, **International Journal of Impact Engineering**, 31:329-339.

[107] Huang, J., Guo, Y., Qin, D., Zhou, Z., Li, D., and Li, Y., 2018, Influence of stress triaxiality on the failure behavior of Ti-6Al-4V alloy under a broad range of strain rates, **Theoretical and Applied Fracture Mechanics**, 97:48-61.

[108] Kang, M., Park, J., Sohn, S. S., Kim, H. S., Kim, N. J., and Lee, S., 2017, Interpretation of quasi-static and dynamic tensile behavior by digital image correlation technique in Twinning Induced Plasticity (TWIP) and low carbon steel sheets, **Materials Science & Engineering A**, 693:170-177.

[109] Moćko, W., and Brodecki, A., 2015, Application of optical field analysis of tensile tests for

calibration of the Rusinek-Klepaczko constitutive relation of Ti6Al4V titanium alloy, **Materials and Design**, 88:320-330.

[110] Li, Y., and Ramesh, K. T., 2007, An optical technique for measurement of material properties in the tension Kolsky bar, **International Journal of Impact Engineering**, 34:784-798.

[111] Song, B., Sanborn, Susan, D., Johnson, K., Dabling, J., Carroll, J., Brink, A., Grutzik, S., and Kustas, A., 2019, Correction of specimen strain measurement in Kolsky tension bar experiments on work-hardening materials, **International Journal of Impact Engineering**, 132:103328.

[112] Song, B., Chen, W., Antoun, B. R., and Frew, D. J., 2007, Flow Stress Obtained on Ductile Specimens Deforming at High Strain Rates, **Experimental Mechanics**, 47:671-679.

[113] Song, B., and Sanborn, B., 2019, A modified Johnson-Cook model for dynamic response of metals with an explicit strain- and strain-rate-dependent adiabatic thermosoftening effect, **Journal of Dynamic Behavior of Materials**, 5:212-220.

[114] Mirone, G., 2013, The dynamic effect of necking in Hopkinson bar tension tests, **Mechanics of Materials**, 58:84-96.

[115] Zhang, L, Gour, G., Petrinic, N., and Pellegrino, A., 2020, Rate dependent behaviour and dynamic strain localisation of three novel impact resilient titanium alloys: experiments and modelling, **Materials Science & Engineering A**, 771:138552.

[116] Jin, H., Sanborn, B., Lu, W.-Y., and Song, B., 2020, Mechanical characterization of 304L-VAR stainless steel in tension with a full coverage of low, intermediate, and high strain rates, **Experimental Mechanics** (submitted).

[117] Bridgman, P.W., 1956, ***Studies in Large Flow and Fracture***, McGraw-Hill.

[118] Ling, Y., 1996, Uniaxial true stress-strain after necking, **AMP Journal of Technology**, 5:37-48.

[119] Mirone, G., 2004, A new model for the elastoplastic characterization and the stress-strain determination on the necking section of a tensile specimen, **International Journal of Solids and Structures**, 41:3545-3564.

[120] Bacha, A., Daniel, D., and Klocker, H., 2007, On the determination of true stress triaxiality in sheet metal, **Journal of Materials Processing Technology**, 184:272-287.

[121] Barton, D.C., 2004, Determination of the high strain rate fracture properties of ductile materials using a combined experimental/numerical approach, **International Journal of Impact Engineering**, 30:1147-1159.